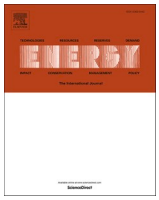
Energy 361 (2026) 142126



Contents lists available at ScienceDirect

Energy

journal homepage: www.elsevier.com/locate/energy





Allowable disturbance ratios of CO_2 flow rate and coal feeding rate for coal-fired supercritical carbon dioxide boiler

Binghan Ma [a], Jinliang Xu [a,b,*], Bin Shen [a], Chuxiong Wang [a], Guanglin Liu [a,b]

[a] Beijing Key Laboratory of Multiphase Flow and Heat Transfer for Low Grade Energy Utilization, North China Electric Power University, Beijing, 100026, China
[b] Key Laboratory of Power Station Energy Transfer Conversion and System (North China Electric Power University), Ministry of Education, Beijing, 102206, China

ARTICLE INFO

Keywords:
Coal-fired boiler
Supercritical CO_2 power plant
Disturbance
Dynamic characteristic

ABSTRACT

Dynamic characteristics of supercritical carbon dioxide boiler is important to ensure safe operation and develop control strategy, but available studies are limited. Here, the supercritical carbon dioxide boiler adapted to a 300 MWe power plant is investigated. To eliminate large pressure drop penalty, modular design is applied to decouple the boiler into ten heat transfer modules. A transient one-dimensional flow and heat transfer model is established in the supercritical carbon dioxide fluid side, coupling a combustion model via thermal conduction across tube wall thickness. Numerical simulations are performed covering the ranges of 30%-100% turbine heat acceptance for base load ratios, and −25%~25% for disturbance ratios of CO_2 flow rate and coal feeding rate with stepwise variation. Dynamic responses of the working fluid side, as well as the maximum allowable disturbance ratios subject to material temperature limit and temperature change rate limit of tube wall are investigated. It is found that temperature variation amplitudes of main steam and reheat steam change quasi-linearly with respect to disturbance ratios of CO_2 and coal. The temperature change rate limit of 5 K/min is found to be a stricter criterion than the material temperature limit to ensure the boiler safety. The allowable disturbance range of CO_2 flow rate expands from (5~6)% at full turbine heat acceptance to (9~10)% at 30% turbine heat acceptance, corresponding to an increase of ~75%, concluding enlarged allowable disturbances for partial load operation. Our work provides new data and insights regarding the boiler safety under disturbance conditions.

1. Introduction

Due to intermittent, random and unstable features of renewable energy sources such as wind and solar, their large-scale integration poses serious challenges to grid safety and stability [1]. These fluctuations can, in principle, be compensated by ultra-large energy storage systems operating over timescales ranging from milliseconds to hours [2]. Unfortunately, no existing energy storage technology can provide such enormous power capacity [3]. Gas-turbine power generation systems exhibit rapid load variation rates, typically 5%~7% Pe/min, and are therefore effective in balancing the variability of renewable energy [4]. In China, natural gas resources are limited, whereas coal resources are abundant [5]. As a result, coal-fired power plants are shifting from base-load power suppliers to flexible and adjustable power sources [6].

Many studies have investigated the flexibility and transient operation of coal-fired power plants (CFPP) based on the Rankine cycle with water-steam as the working fluid [7]. Several parameters are commonly used to characterize CFPP flexibility, including the minimum load ratio and load variation rate [8], start-up and shut-down time [9], and the dynamic response to parameter disturbances [10]. Due to large thermal inertia of CFPP, their response to external load variations or parameter disturbances is relatively slow [11]. Currently, the load variation rate is ~2%Pe/min [12], which is still insufficient to balance renewable energy. However, further enhancing flexibility may introduce serious safety issues. Flameout may occur under ultra-low-load operation [13]. Thermal stress may cause component deformation and also lead to fatigue damage in thick-walled pressure vessels [14]. To further improve CFPP flexibility, the integration of an additional thermal energy storage system has been proposed [15].

Here, we explore the potential of using the supercritical carbon dioxide (sCO_2) cycle to achieve higher flexibility without incorporating an additional thermal energy storage system. Compared with the Rankine

* Corresponding author. Beijing Key Laboratory of Multiphase Flow and Heat Transfer for Low Grade Energy Utilization, North China Electric Power University, Beijing, 100026, China.
E-mail address: xjl@ncepu.edu.cn (J. Xu).

https://doi.org/10.1016/j.energy.2026.142126
Received 7 December 2025; Received in revised form 14 April 2026; Accepted 31 July 2026
Available online 1 August 2026
0360-5442/© 2026 Elsevier Ltd. All rights are reserved, including those for text and data mining, AI training, and similar technologies.

cycle systems, the sCO_2 coal-fired power plants offer higher efficiency and greater flexibility [16]. Several studies have investigated the integration of the sCO_2 boiler with the cycle. At the same capacity, the mass flow rate in a sCO_2 boiler is about 6~8 times that in a conventional water-steam boiler, resulting in a much larger pressure drop. Under such conditions, conventional boiler designs would reduce cycle efficiency. To address this issue, Xu et al. [17] proposed a modular design for the sCO_2 boiler in which the module length and mass flow rate were both reduced by half, thereby substantially lowering the pressure drop. Sun et al. [18] introduced a novel combined cycle (Connected-top-bottom-cycle), which enables full utilization of flue gas over the entire temperature range. They further applied the overlap energy utilization principle to balance the efficiencies of the top and bottom cycles [19]. Another important challenge is maintaining the cooling wall temperature at an acceptable level, because the CO_2 entering the cooling walls has a relatively high temperature and the heat transfer coefficient of CO_2 inside the tubes is limited [20]. To reduce the wall temperature, Liu et al. [21] proposed four measures: improved coupling in furnace width direction, flue gas recirculation for heat flux reduction, improved coupling in furnace height direction, and enhanced heat transfer in cooling wall tubes. These studies were all conducted under steady state conditions.

However, studies on dynamic conditions for sCO_2 coal-fired power generation systems remain limited. Liu et al. [22] established a dynamic model for a sCO_2 boiler and compared its transient behaviors with those of a water-steam supercritical boiler under disturbances, showing that the sCO_2 boiler has a faster response. Ma et al. [23] investigated the transient characteristics of cooling wall in a sCO_2 coal-fired boiler during load variations at different load variation rates. To better understand disturbance effects under flexible operation, related studies on conventional water-steam boiler also provide useful reference. Kim and Choi [24] developed a one-dimensional dynamic model for a supercritical once-through boiler and analyzed how heat flux and mass flow disturbances affect the transient evolution of thermal-hydraulic parameters. Wang et al. [25] investigated the water-cooled wall of an ultra-supercritical boiler and showed that the sensitivity of outlet steam temperature to feedwater temperature, feedwater mass flow rate, and heat load disturbances changes with load condition. Zhu et al. [26] revealed that as the calorific value of coal increases, the main steam temperature can maintain at the design value with attempering water adjustments. Guo et al. [27] reported different disturbance sources can produce different response magnitudes and response times at different heating surface locations. Tao et al. [28] indicated that low load operation weakens the flow stability of the water-cooled wall. Li et al. [29] showed that sudden flow rate reduction can rapidly aggravate wall temperature, deformation, and stress in the water-cooled wall.

For a sCO_2 coal-fired boiler, the inlet CO_2 temperature is ~150 °C higher than that in a conventional water-steam boiler. Meanwhile, the CO_2 in the boiler is far from the pseudo-critical point, and the convective heat transfer coefficient inside the tubes is relatively low. As a result, the tube wall temperature of sCO_2 boiler is generally high. Therefore, wall temperature and temperature change rate are two important safety indexes. The wall temperature determines whether the material temperature limit is exceeded. Excessive wall temperatures can accelerate high temperature corrosion, leading to gradual thinning of the tube walls and potentially resulting in rupture of the heating surfaces, thereby posing a serious threat to the safe operation of the unit [30]. The temperature change rate dominates the internal temperature gradients, especially during startup, shutdown, or rapid load changes, and these gradients drive the development of thermal stresses and potential thermal fatigue [31]. If the temperature varies too rapidly, non-uniform temperature fields form inside the material and then induce thermal stress. A strict limit of 5 K/min has been adopted in sCO_2 systems as an index [23,32,33], it is also adopted here as a criterion to evaluate the boiler safety.

In summary, previous disturbance studies on conventional water-steam boilers mainly focused on working fluid side transient responses, or on tube wall side safety of some local heating surfaces. For coal-fired sCO_2 boilers, the available dynamic studies mainly focused on working fluid side responses under disturbances at the rated condition, or focused on the effect of load variation rate on the transient characteristic from one steady state to another steady state. However, for safe and flexible operation, it remains unclear under different load ratios what the allowable disturbance limits of CO_2 flow rate and coal feeding rate are in the entire sCO_2 boiler. These disturbance limits should ensure wall temperature and temperature change rate within safe limits in all heating surfaces. Therefore, it is necessary to quantitatively determine the allowable disturbance limits of CO_2 flow rate and coal feeding rate under different load ratios.

To address this issue, a dynamic model of a 300 MW coal-fired sCO_2 modular boiler is developed by coupling the working fluid side with the combustion side. Stepwise disturbances in CO_2 flow rate and coal feeding rate are imposed under different load ratios. The main objectives of this study are to: (1) analyze the transient responses of key working fluid side parameters, particularly the variation amplitudes and response times of main steam and reheat steam temperatures under disturbances; (2) determine the allowable disturbance ratios based on the material temperature limit and the temperature change rate limit under different load ratios. The results indicate that the temperature change rate limit is more restrictive than the material temperature limit, and the partial load operation enlarges the allowable disturbance ratios. These findings provide useful guidance for the safe and flexible operation of sCO_2 boilers.

2. Model and methods

In this work, a 300 MW sCO_2 coal-fired power system based on the connected-top-bottom-cycle is adopted [18], together with the overlap energy utilization principle [19]. As shown in Fig. 1, the top cycle adopts a single-reheat recompression configuration (RC + RH), whereas the bottom cycle adopts a recompression reheat cycle integrated with an external air preheater (RC + RH + EAP). Several key components in the top and bottom cycles operate at the same temperature and pressure, which makes component integration possible. The main design parameters of the cycle are summarized in Table 1. The system consists of several key components, including the high-pressure turbine (T1), low-pressure turbine (T2), high temperature recuperator (HTR), low temperature recuperator (LTR), main compressor (C1), auxiliary compressor (C2), cooler and boiler.

During operation, CO_2 first expands in T2 and is then divided between the top and bottom cycles. In the top cycle, energy is recovered through the HTR and LTR. Part of the flow is directed to the C2 for pressurization, while the remaining portion passes through the C1 branch. After passing through the LTR, this stream merges with the outlet stream from C2 in the top cycle, absorbs heat, and reaches state point 5a. Meanwhile, the other portion of the fluid enters the bottom cycle, where it absorbs heat and reaches state point 5b. Finally, the CO_2 from 5a and 5b are recombined and enter T1 for expansion. The fluid then passes through reheater for further heat absorption before returning to T2, thereby accomplishing the cycle.

2.1. Model of supercritical carbon dioxide boiler

The boiler adopts a π-type layout with a four-corner tangential firing system, and the furnace has a square cross-section. The heating surfaces are arranged according to the modular design, as illustrated in Fig. 2. In this configuration, both the module length and the working fluid velocity are half of their original values. Since the frictional pressure drop is proportional to the square of the flow velocity and to the flow path length, the pressure drop is only 1/8 of the original value. The primary heater (Heater 1) consists of Part 1 and SH1, together with Part 2 and SH2, whereas the reheater (Heater 2) consists of LRH1, HRH1, LRH2, and HRH2. Heater 1 and Heater 2 jointly supply heat to the working

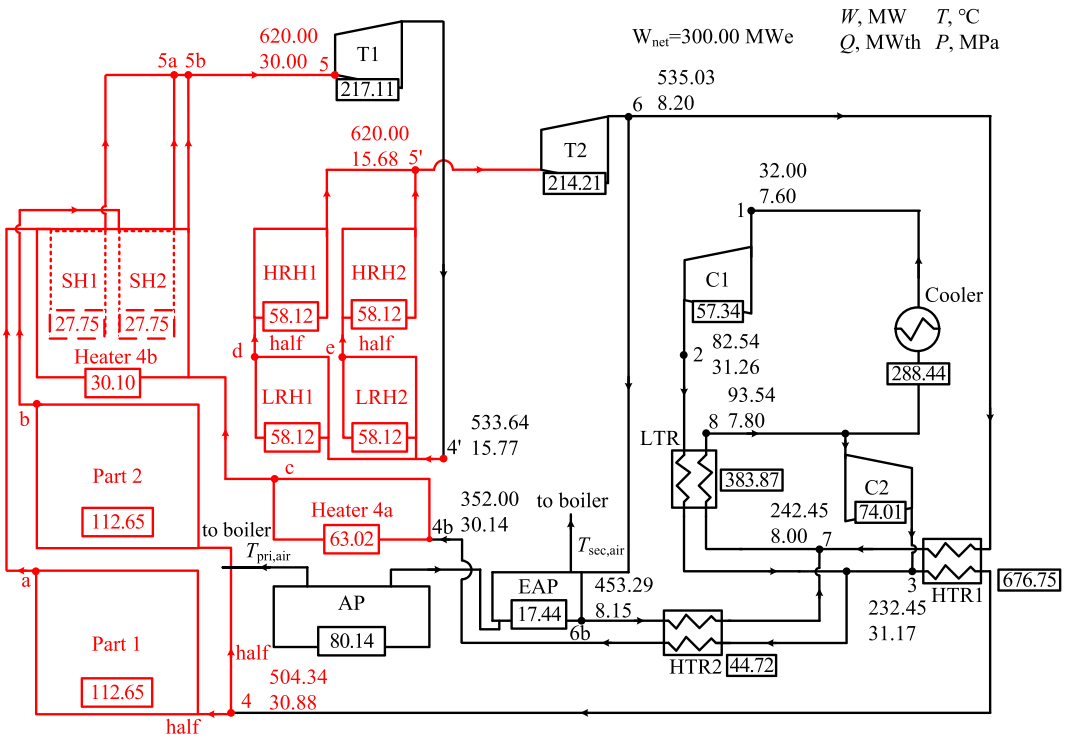


Fig. 1. Coal-fired sCO_2 power generation system.

Table 1
Main parameters of sCO_2 cycle at the rated condition (100%THA).

State points	Pressure/MPa	Temperature/°C	Mass flow rate/t/h
1	7.60	32.00	5282.32
2	31.26	82.54	5282.32
3	31.17	232.45	6857.51
4	30.88	504.34	6857.51
4b	30.14	352.00	983.93
5	30.00	620.00	7841.45
4′	15.77	533.64	7841.45
5′	15.68	620.00	7841.45
6	8.20	535.03	7841.45
6b	8.15	453.29	660.32
7	8.00	242.45	7841.45
8	7.80	93.54	7841.45

fluid in the top cycle, while Heater 2 also provides heat to the bottom cycle. In addition, Heater 4a and Heater 4b are connected in series to supply heat exclusively to the bottom cycle.

The heat flux distribution along the furnace height and the tube arrangements in different modules are illustrated in Fig. 3. Heat transfer in the furnace is dominated by radiation, and the local heat flux is approximately proportional to the fourth-power of the temperature difference between the flue gas and the outer wall of the cooling tubes. Owing to the extremely high flue gas temperature in the furnace, the heat flux variation is governed mainly by the flue gas temperature distribution. Since the sCO_2 boiler exhibits a similar geometry and combustion layout with conventional steam boilers, the vertical non-uniformity of heat flux distribution is determined using the empirical profile commonly adopted in steam-boiler design [34].

Part 1, Part 2, and Heater 4b are arranged along the furnace cooling wall, and their structural configurations are shown in Fig. 3b [16]. SH1 and SH2 are located at the furnace roof, together with the preceding modules, serve as radiation heating surfaces. HRH1 and HRH2 are arranged in the horizontal flue, whereas LRH1, LRH2 and Heater 4a are installed in the tail flue. These modules act as convective heating surfaces. The structural configurations of SH1, SH2, and the other heating

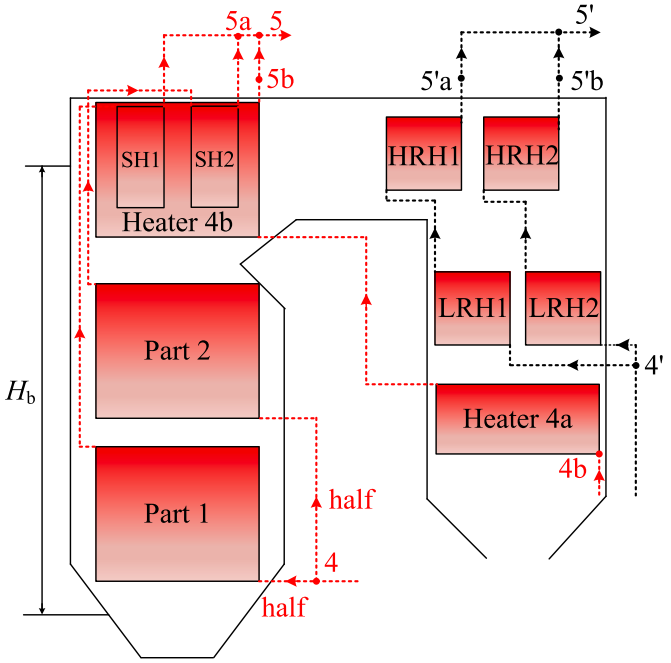


Fig. 2. Modular design of the sCO_2 boiler.

surfaces are illustrated in Fig. 3c. The detailed geometric parameters and the corresponding materials of each module are listed in Table 2. By coupling all the modules, the dynamic model of the sCO_2 boiler is established. The properties of the coal utilized in the boiler are listed in Table 3, where Q_{LHV} represents the lower heating value of the coal on an as-received basis.

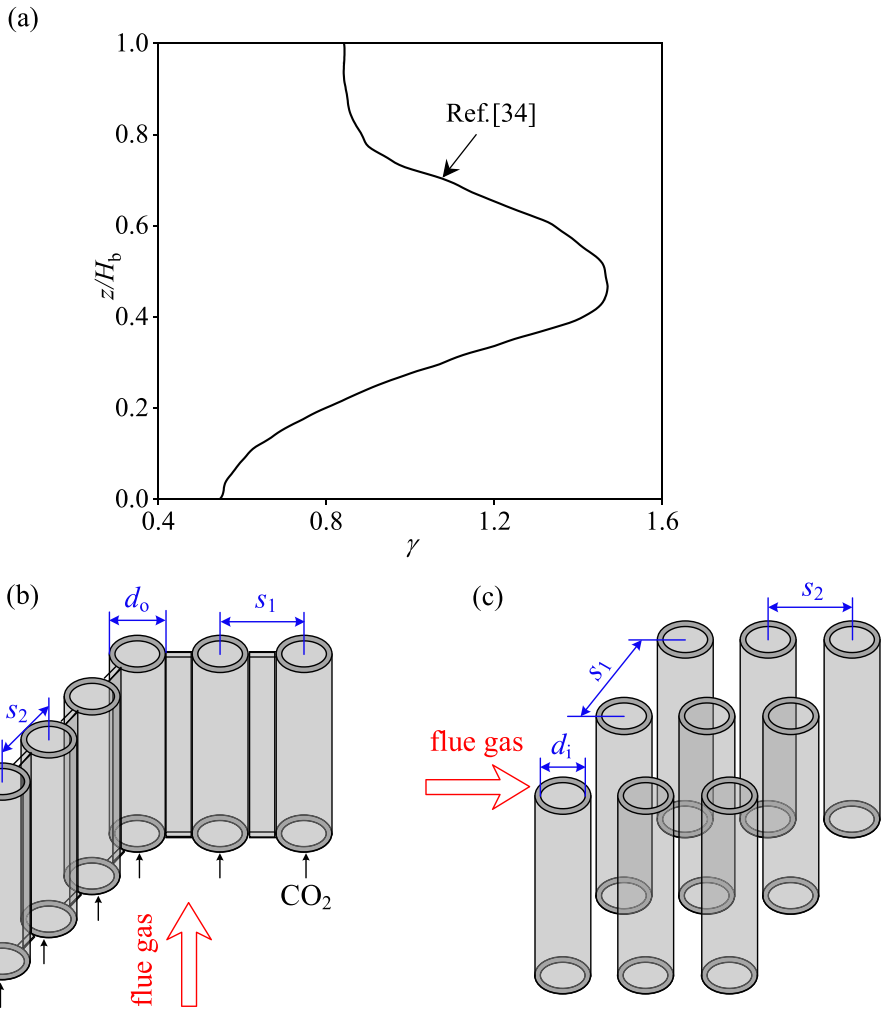


Fig. 3. Non-uniform distribution of heat fluxes in the furnace height direction (a) and the heater surface arrangement (b) and (c), cited from Ref. [16], Copyright 2020, Elsevier.

Table 2
Geometric parameters and materials of heat transfer modules.

Heat exchange modules	$d_i \times \delta_w$/mm	s_1/mm	s_2/mm	Material
Part 1	24×8	56	-	Super304H
Part 2	24×8	56	-	Super304H
Heater 4b	20×6	45	-	Super304H
SH	32×8	1350	60	Super304H
HRH	35×5	450	60	Super304H
LRH	48×5.5	120	74	T91
Heater 4a	25×7.3	80	79	12Cr1MoVG

2.2. Numerical model

A modular dynamic model of the sCO_2 boiler was established in Aspen Custom Modeler (ACM) to capture the transient thermodynamic and heat transfer behavior under disturbance conditions. The model comprises three coupled subsystems: (i) the working fluid side; (ii) the combustion side; and (iii) the tube wall thermal conduction model, which provides two side thermal coupling between the working fluid and the flue gas. The present study focuses on the component-level dynamic response of the sCO_2 boiler, particularly the transient responses of the working fluid and tube wall under disturbances. Since coal combustion occurs on a much shorter timescale than the boiler side thermal response, combustion reaction kinetics have been neglected in some previous dynamic boiler studies as a simplified treatment [35,36]. Existing studies have demonstrated that this treatment can still provide satisfactory agreement with industrial operating data [35]. Since the objective of the present work is to investigate the dynamic responses of boiler components rather than the detailed combustion process, combustion reaction kinetics are also neglected here to avoid the substantial computational burden of a fully coupled combustion model. On this basis, the following simplifying assumptions are adopted: (1) The coal composition remains constant. (2) The combustion reaction kinetics are neglected. (3) Axial heat conduction along the tube wall is neglected. (4) Both the working fluid and flue gas flows are modeled as one-dimensional along the axial direction.

2.2.1. Working fluid side model

The transient thermodynamic and hydrodynamic behaviors of CO_2

Table 3
Properties of the designed coal.

C_{ar}	H_{ar}	O_{ar}	N_{ar}	S_{ar}	A_{ar}	M_{ar}	V_{daf}	Q_{LHV}
61.70%	3.67%	8.56%	1.12%	0.60%	8.80%	15.55%	34.73%	23442 kJ/kg

inside the boiler tubes are governed by the time-dependent conservation equations of mass, momentum, and energy [37]. These equations form the foundation of the one-dimensional transient working fluid side model and provide the basis for the subsequent analyses of pressure drop, heat transfer, and thermal coupling.

Mass conservation:

$$\frac{\partial \rho}{\partial t}+\frac{\partial(\rho v)}{\partial z}=0 \tag{1}$$

Momentum conservation:

$$\frac{\partial(\rho v)}{\partial t}+\frac{\partial(\rho v^2)}{\partial z}=-\frac{\partial P}{\partial z}-\frac{\partial P_f}{\partial z}-\rho g \tag{2}$$

Energy conservation:

$$\frac{\partial(\rho h)}{\partial t}+\frac{\partial(\rho v h)}{\partial z}=\frac{\partial P}{\partial t}+Q_f \tag{3}$$

where ρ, v and h denote the CO_2 density, velocity and specific enthalpy, respectively; P is the pressure; g is the gravity acceleration; Q_f is the heat source term representing the heat absorbed by CO_2.

The frictional pressure drop is obtained using the Darcy-Weisbach equation [38]:

$$\frac{\partial P_f}{\partial z}=\frac{f}{d_i}\cdot\frac{\rho v^2}{2} \tag{4}$$

where d_i is the inner tube diameter.

The friction coefficient f is determined using the empirical correlation [39]:

$$f=\frac{1}{3.24\,\lg^2\left[\left(\frac{\Delta/d_i}{3.7}\right)^{1.1}+\frac{6.9}{Re_f}\right]} \tag{5}$$

where Δ denotes the absolute roughness of the tube wall [40] and Re_f represents the Reynolds number of the working fluid.

Existing heat transfer correlations that consider buoyancy and acceleration effects still exhibit considerable deviations from experimental observations [41]. To improve predictive accuracy, substantial efforts have been devoted to the development of more reliable heat transfer correlations. Based on the heat transfer mechanism associated with the thickness of the wall attached vapor-like layer, a dimensionless K number was introduced to characterize the competition between evaporation induced momentum force and inertial force, thereby quantifying the effect of the vapor-like layer. On this basis, a generalized heat transfer correlation was proposed by incorporating the K term in addition to the Reynolds and Prandtl numbers [42].

A total of 5560 data points were used in the development of this correlation, including 2028 data points obtained from our experiments and 3532 data points collected from 18 published studies, covering three working fluids of CO_2, H_2O, and R134a. The predictive performance of the K number correlation was further evaluated against five existing correlations, including those proposed by Bishop et al. [43], Jackson [44], Jackson and Hall [45], Yu et al. [46], and Gupta et al. [47], in terms of both the Nusselt number and inner wall temperature. The corresponding error indices, including the mean relative error (e_A), mean absolute relative error (e_R), and root-mean-square error (e_S), were summarized. For all three working fluids, the K number correlation achieved the highest prediction accuracy, indicating a clear advantage over the other correlations. The detailed expressions are given as follows:

$$\alpha_f=\frac{Nu\cdot\lambda_f}{d_i} \tag{6}$$

where λ_f is the thermal conductivity of the working fluid. The Nusselt number, Nu, is calculated as follows:

$$Nu=0.0012Re_f^{0.9484}Pr_{f,ave}^{0.718}K^{-0.0313} \tag{7}$$

$$Re_f=\frac{G\cdot d_i}{\mu_f},Pr_{f,ave}=\frac{\mu_f\cdot c_{ave}}{\lambda_f},c_{ave}=\frac{h_{wi}-h_f}{T_{wi}-T_f} \tag{8}$$

$$K=\left(\frac{q_{in}}{G\cdot h_{wi}}\right)^2\frac{\rho_f}{\rho_{wi}} \tag{9}$$

where Pr is the Prandtl number. The subscript f denotes that the thermophysical properties are evaluated using the working fluid temperature, while the subscript ave represents the average value. G is the mass flux and μ is the dynamic viscosity. q_{in} represents the inner wall heat flux. The subscript wi indicates that the corresponding properties are evaluated using the inner wall temperature.

2.2.2. Combustion side model

The combustion side model is used to determine the heat input from the flue gas to the tube wall. It is established based on the classical Russian CKTI normative thermal calculation method for coal-fired boilers [48], in which the furnace heat release and heat absorption are determined through the boiler heat balance. The effective heat available from fuel combustion is obtained after deducting the principal heat losses. The effective heat input during combustion is expressed as:

$$Q_{ef}=\left(1-\frac{q_3+q_6}{100-q_4}\right)Q_{LHV}+Q_a \tag{10}$$

where q_3, q_4 and q_6 represent the heat losses due to chemical incomplete combustion, mechanical incomplete combustion, and sensible heat of ash and slag, respectively. Q_{LHV} is the lower heating value of coal; Q_a is the thermal input from preheated air.

Since the present study focuses on the component-level dynamic characteristics of the sCO_2 boiler under parameter disturbances, the heat input to the radiation heating surfaces is determined based on the overall furnace heat balance, namely from the difference between the effective heat released during combustion and the heat carried by the flue gas at the furnace outlet. This treatment has been commonly used in studies of sCO_2 boiler design [49], off-design analysis [50], and dynamic performance evaluation [51], and previous validations against boiler operating data have shown that it can provide satisfactory accuracy in predicting key outlet parameters [51]. Therefore, the average furnace heat flux is determined by:

$$q_{ave}=\frac{\phi\cdot(Q_{ef}-h_{fg,o})\cdot B}{A_b} \tag{11}$$

where $h_{fg,o}$ is the enthalpy of the flue gas at the furnace outlet; B is the coal feeding rate; A_b is the effective radiative area; ϕ is the heat retention coefficient:

$$\phi=1-\frac{q_5}{\eta_b+q_5} \tag{12}$$

where q_5 is the boiler heat loss and η_b denotes the boiler efficiency.

Local heat flux on the cooling wall is represented by:

$$q=q_{ave}\cdot\gamma \tag{13}$$

where γ is the non-uniformity coefficient along the furnace height.

For the convective heating surfaces arranged as inline tube bundles, the heat exchange between the flue gas and the working fluid is represented by a node-based energy transfer network, as schematically illustrated in Fig. 4. The flue gas is assumed as one-dimensional flow along the gas side flow path, and its mass and energy conservation are given by:

$$\frac{\partial \rho_{fg}}{\partial t}+\frac{\partial(\rho_{fg}v_{fg})}{\partial z}=0 \tag{14}$$

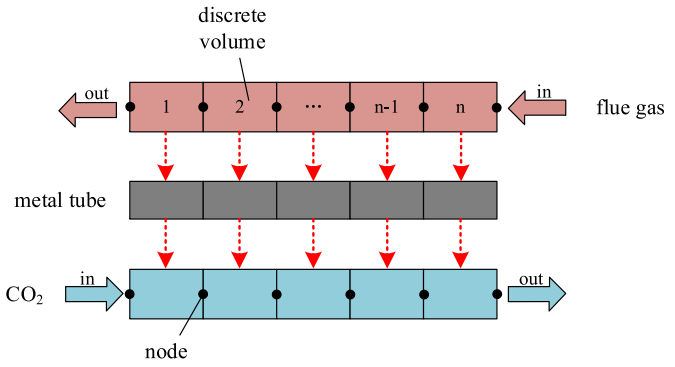


Fig. 4. One-dimensional model for heat transfer between flue gas and CO_2 across tube wall.

$$\frac{\partial(\rho_{fg}h_{fg})}{\partial t}+\frac{\partial(\rho_{fg}v_{fg}h_{fg})}{\partial z}=Q_{fg} \tag{15}$$

where ρ_{fg}, v_{fg} and h_{fg} denote the density, velocity, and enthalpy of the flue gas, respectively; Q_{fg} is the heat source term representing the heat released by the flue gas. The convective heat transfer coefficient on the flue gas side is evaluated using a correlation appropriate for inline tube bundle configurations [52]:

$$\alpha_{fg}=0.2C_sC_z\frac{\lambda_{fg}}{d_o}Re_{fg}^{0.65}Pr_{fg}^{0.33} \tag{16}$$

where C_s is the correction coefficient for the tube bundle geometric arrangement, and C_z represents the correction coefficient for the number of tube rows along the flue gas flow direction.

2.2.3. Tube wall thermal conduction model

In dynamic boiler studies, it is common to model not only the working fluid side but also the tube wall as dynamic element. The tube wall plays an important role during transient processes because its finite heat capacity and transient heat conduction introduce thermal inertia [53]. In addition, tube wall conduction is required to capture the temperature difference and heat conduction through the wall thickness. These effects lead to a thermal lag between furnace side heat input disturbances and the working fluid response, and further effects wall temperature evolution [54], thermal stress, and allowable load ramp rates [23]. Therefore, the transient heat conduction in the tube wall is included in the present study.

The radial temperature distribution in the tube wall is obtained from the transient heat conduction equation [35]:

$$\rho_w c_w\frac{\partial T_w}{\partial t}=\frac{1}{r}\frac{\partial}{\partial r}\left(\lambda_w r\frac{\partial T_w}{\partial r}\right) \tag{17}$$

the boundary condition at the outer wall is:

$$-\lambda_w\frac{\partial T_w}{\partial r}\bigg|_{r=ro}=\alpha_{fg}(T_{fg}-T_{wo}) \tag{18}$$

and at the inner wall:

$$-\lambda_w\frac{\partial T_w}{\partial r}\bigg|_{r=ri}=\alpha_f(T_{wi}-T_f) \tag{19}$$

where ρ_w, c_w, λ_w are the tube wall density, heat capacity, and thermal conductivity. These equations provide the thermal coupling between the working fluid side and combustion side subsystems.

2.3. Calculation procedure

The calculation procedure for the transient simulation of the modular sCO_2 coal-fired boiler is shown in Fig. 5. The procedure firstly defines the thermodynamic cycle and boiler design parameters. Based on these inputs, the integrated design of the sCO_2 coal-fired power generation system and its components is carried out to obtain the state point parameters at 100%THA, along with the boiler geometry and heater module data [16]. Subsequently, the partial-load calculation process is executed to determine the thermodynamic state parameters of the system under different load ratios [50].

A dynamic model of the modular sCO_2 boiler is then established in ACM. The thermophysical properties of CO_2 are obtained from the Aspen built-in property database. The thermo-physical properties of the wall material, including density, heat capacity, and thermal conductivity, are treated as temperature-dependent and are evaluated using fitted correlations based on the material data listed in Table 4. Each heating module is discretized along the flow direction using the finite-difference method, transforming the governing partial differential equations into a set of differential algebraic equations to capture the distributed thermal-hydraulic behavior. The resulting system is solved using the implicit Euler method to ensure numerical stability. The axial spatial step size is set to 0.5 m, and its adequacy has been verified in previous work through a grid-independence test [23]. A fixed time step of 0.2 s is employed, and the solver convergence tolerance in ACM is set to 0.0001 to guarantee adequate numerical accuracy. For each load ratio, the corresponding steady state parameter distributions of the boiler are used as the initial conditions. The inlet temperature, pressure, and mass flow rate of CO_2, together with the coal feeding rate, are specified as the boundary conditions. Step disturbances are then imposed on the CO_2 flow rate and the coal feeding rate. The corresponding transient variations in outlet parameters of the main and reheat steam and the tube wall temperatures of each module are analyzed to characterize the dynamic response of the boiler.

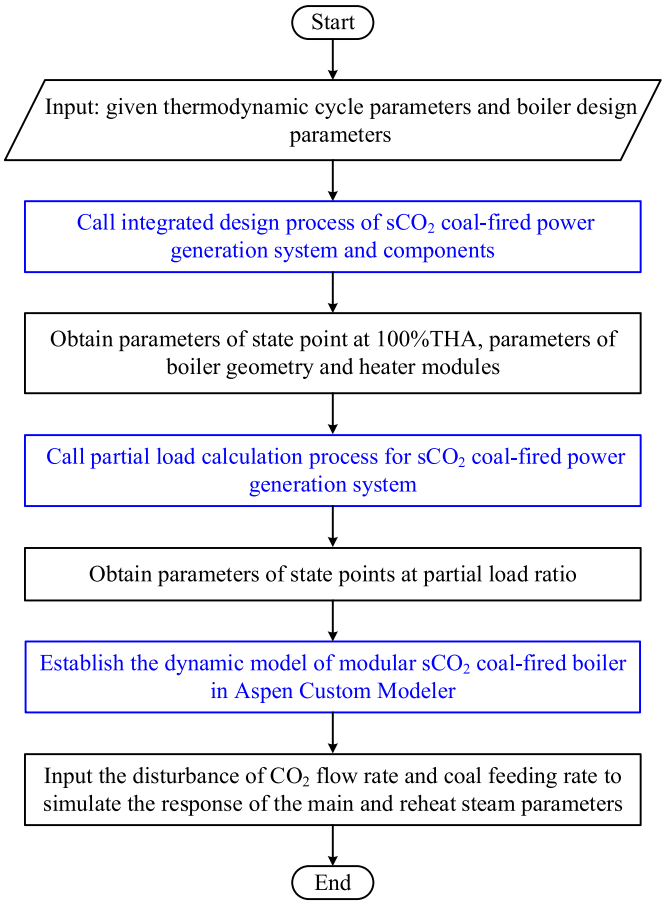


Fig. 5. The calculation procedure for transient simulation of sCO_2 boiler.

Table 4
Physical properties of material.

Material	T/°C	100	300	500	600	700	800
Super304H	density/kg/m^3	7940	7940	7940	7940	7940	7940
	thermal conductivity/W/(m·K)	16.2	21.5	25.2	28.6	31	31
	specific heat capacity/kJ/(kg·K)	0.511	0.618	0.658	0.716	0.733	0.707
T91	density/kg/m^3	7780	7780	7780	7780	7780	7780
	thermal conductivity/W/(m·K)	27	29.2	29	29.3	29	29
	specific heat capacity/kJ/(kg·K)	0.469	0.511	0.540	0.580	0.800	0.850
12Cr1MoVG	density/kg/m^3		7800	7800	7800		
	thermal conductivity/W/(m·K)		42.7	37.7	35.5		
	specific heat capacity/kJ/(kg·K)		0.611	0.682	0.729		

2.4. Model validation

Since the 300 MW coal-fired sCO_2 boiler has not yet been put into operation, the dynamic model cannot be validated using operating data. To ensure the reliability of the developed model, a two-stage validation is adopted, consisting of steady state verification under multiple load ratios and performs transient validation using transient numerical results reported in published studies.

First, a steady state consistency check was performed at 100% THA, 75% THA, and 50% THA by comparing the ACM results with the corresponding boiler thermal calculation results at the same load. Here, the "thermal calculation data" refer to the steady state results obtained from the boiler design [16] and off-design partial load calculation procedure [50] described in Section 2.3. Since a standard design calculation procedure for sCO_2 coal-fired boilers is not yet available, the present thermal calculation was carried out using the conventional design method for water-steam boilers, which has been developed over a long period and widely validated in boiler thermal design [52,55]. In contrast, the "simulated results" refer to the results of the ACM model, in which the module geometry is retained and the corresponding load-dependent boundary conditions are specified. The model is then solved under steady state conditions and the outlet temperatures and pressures are extracted for comparison. The outlet temperature and pressure of Part 1 and LRH1, as well as those of the main and reheat steam, were selected as representative variables. As summarized in Table 5, the ACM results agree closely with the corresponding thermal calculation data, indicating that the steady state thermal hydraulic behavior of the modular boiler is accurately captured.

Second, the transient prediction capability of the model has been verified in our previous work [23], where the numerical results reported in Ref. [56] were successfully reproduced. In that study, the transient fluid-solid coupling behavior of the furnace cooling wall tube was simulated using the same boundary conditions: a mass flow rate of 0.821 kg/s, an inlet temperature of 315 °C, and an inlet pressure of 29.9 MPa, as well as the height-dependent heat flux distribution provided in the reference. For the transient validation, the heat flux was applied to the tube at $t = 0$ s, and the temporal evolution of the temperature at the center of the fire-facing side of the tube wall and the fin temperature were compared. The maximum deviation of the fin temperature was only 1.87%, demonstrating that the developed model can accurately capture the dynamic thermal response of the heating surfaces. By combining steady state validation across multiple load ratios with transient verification based on benchmark data from literature, the accuracy of the sCO_2 boiler dynamic model is comprehensively confirmed.

Table 5
Comparison between simulated results and thermal calculation data.

Parameters	Thermal calculation data	Simulated results	Relative error
		100%THA	
Part 1 outlet temperature/°C	597.51	596.86	−0.11%
Part 1 outlet pressure/MPa	30.68	30.71	0.10%
Main steam temperature/°C	620.00	620.40	0.06%
Main steam pressure/MPa	30.00	29.93	−0.23%
LRH1 outlet temperature/°C	576.99	578.17	0.20%
LRH1 outlet pressure/MPa	15.70	15.69	−0.06%
Reheat steam temperature/°C	620.00	619.55	−0.07%
Reheat steam pressure/MPa	15.69	15.68	−0.06%
		75%THA	
Part 1 outlet temperature/°C	601.41	601.01	−0.07%
Part 1 outlet pressure/MPa	25.79	25.82	0.12%
Main steam temperature/°C	620.00	621.52	0.25%
Main steam pressure/MPa	25.25	25.16	−0.36%
LRH1 outlet temperature/°C	569.31	569.89	0.10%
LRH1 outlet pressure/MPa	13.63	13.64	0.07%
Reheat steam temperature/°C	606.64	605.65	−0.16%
Reheat steam pressure/MPa	13.62	13.63	0.07%
		50%THA	
Part 1 outlet temperature/°C	605.38	605.49	0.02%
Part 1 outlet pressure/MPa	21.38	21.40	0.09%
Main steam temperature/°C	620.00	619.52	−0.08%
Main steam pressure/MPa	20.94	20.88	−0.29%
LRH1 outlet temperature/°C	568.68	565.48	−0.56%
LRH1 outlet pressure/MPa	11.89	11.90	0.08%
Reheat steam temperature/°C	599.78	594.28	−0.92%
Reheat steam pressure/MPa	11.88	11.89	0.08%

3. Results and discussion

The definitions of the disturbance input, response metrics, and safety criteria are summarized in Fig. 6. As illustrated in Fig. 6a, the disturbed variable (σ) has an initial value of σ_s, where σ represents either the mass flow rate of CO_2 (m_{CO2}) or the coal feeding rate (m_{coal}). A step disturbance with an amplitude of φ is imposed at time t_d. The disturbance ratio (δ) is defined as $\delta = \varphi/\sigma_s$ for a positive disturbance and $\delta = -\varphi/\sigma_s$ for a negative disturbance. As shown in Fig. 6b, the temperature variation amplitudes of the main steam and reheat steam are defined as ΔT_5 and

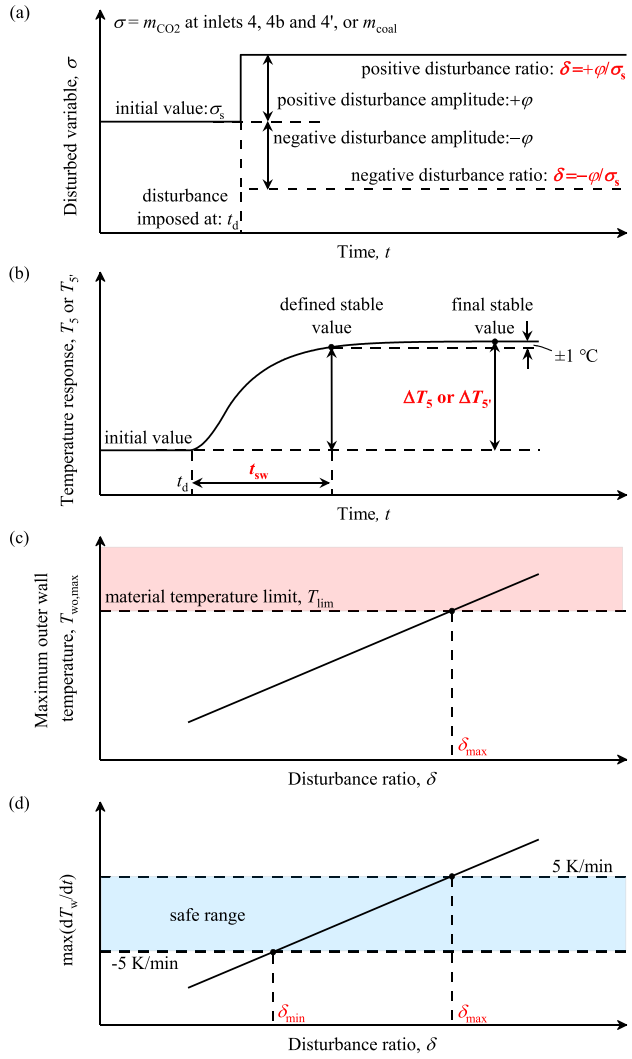


Fig. 6. Definition of (a) disturbance input, (b) response metrics, (c) and (d) safety criteria for the problem.

$\Delta T_{5'}$, respectively. While the response time (t_{sw}) is defined as the time interval from t_d to the instant when the temperature enters the ±1 °C band around the final steady state value [22,57]. In addition, Fig. 6c defines the allowable disturbance limit determined by the material temperature limit ($T_{wo,max} = T_{lim}$), and Fig. 6d defines the allowable disturbance range determined by the wall temperature change rate criterion of ±5 K/min, giving the lower and upper limits, δ_{min} and δ_{max}.

3.1. Dynamic characteristics of the boiler under step disturbance of CO_2 flow rate

At $t = 500$ s, a step disturbance of +5% was applied to the total CO_2 mass flow rate entering the boiler, corresponding to state points 4, 4b, and 4′ in the system. The variations in the temperatures, pressures and mass flow rates of the main and reheat steam are illustrated in Fig. 7, where the time axis is plotted on a logarithmic scale for clarity. Both the main steam and reheat steam temperatures gradually decreased. This behavior is attributed to the fact that the heat flux remained constant, whereas the heat absorbed per unit mass of CO_2 decreased as the mass flow rate increased. The main steam temperature eventually decreased by 6.2 °C, with a response time of ~130 s, whereas the reheat steam temperature decreased by 3.9 °C, with a similar response time of ~130 s. Both the main and reheat steam pressures decreased immediately after the disturbance, although the magnitudes were relatively small. The main steam pressure dropped by ~0.1 MPa, while the reheat steam pressure decreased by ~0.01 MPa. This result indicates that the disturbance mainly affects the thermal state rather than the pressure level. The sudden increase in mass flow rate raised the flow velocity, thereby increasing the frictional pressure drops along the pipelines and causing a rapid pressure reduction at the outlet. Meanwhile, the mass flow rates of both the main and reheat steam rose sharply after the disturbance, consistent with the principle of mass conservation. For supercritical water-steam boiler, the temperature and mass flow rate respond much more slowly to inlet flow rate disturbances than those in sCO_2 boilers [11]. This slower response mainly arises because the heating, evaporation, and superheating sections require time to re-establish thermal equilibrium after the disturbance. The redistribution of heat absorption among these sections further delays the change in outlet conditions. In contrast, CO_2 in the sCO_2 boiler remains single phase state and has much lower thermal inertia, which enables a significantly faster dynamic response.

The variation amplitudes and response times under different disturbance ratios at 100%THA are analyzed. As shown in Fig. 8a, the variation amplitudes of both the main steam and reheat steam change approximately linearly with the disturbance ratio of CO_2 flow rate (δ_{mCO2}). This behavior is mainly attributed to the fact that, within the investigated disturbance range, the change in CO_2 mass flow rate causes an approximately proportional change in the heat absorbed per unit mass of working fluid, thereby resulting in an approximately linear outlet temperature response. Positive flow rate disturbances lead to temperature decreases, whereas negative disturbances cause temperature increases. Specifically, when $\delta_{mCO2} = +10\%$, ΔT_5 and $\Delta T_{5'}$ are −11.8 °C and −7.5 °C, respectively; when $\delta_{mCO2} = -10\%$, they increase to 14.1 °C and 9.1 °C, respectively. Therefore, for the same disturbance magnitude, the temperature response of the main steam is consistently larger than that of the reheat steam, indicating that the main flow path is more thermally sensitive to inlet flow rate disturbances. In addition, a slight asymmetry is observed in the response. Compared with the corresponding positive disturbance, the temperature rise under a −10% disturbance is larger by 2.3 °C for the main steam and 1.6 °C for the reheat steam.

Fig. 8b illustrates the variation of t_{sw} with δ_{mCO2}. t_{sw} of both T_5 and $T_{5'}$ increase with $|\delta_{mCO2}|$, and the corresponding curves are approximatively symmetrical against the zero-deviation line. However, the sensitivities of the two temperatures are clearly different. For T_5, t_{sw} increases slowly when $|\delta_{mCO2}| \leq 6\%$, reaching ~160 s at $\delta_{mCO2} = +6\%$ and ~190 s at $\delta_{mCO2} = -6\%$. However, it rises sharply once $|\delta_{mCO2}| > 6\%$, reaching ~1220 s at $\delta_{mCO2} = +10\%$ and ~1400 s at $\delta_{mCO2} = -10\%$. In contrast, the response of $T_{5'}$ is much milder and exhibits an approximately parabolic dependence on $|\delta_{mCO2}|$. At $|\delta_{mCO2}| = 10\%$, t_{sw} is only ~190 s for +10% and ~260 s for −10%. When $|\delta_{mCO2}| \leq 6\%$, t_{sw} of T_5 and $T_{5'}$ are comparable; however, as $|\delta_{mCO2}|$ increases, the main steam shows a much longer delay in temperature stabilization. This difference arises from the larger thermal inertia of Heater 4a and Heater 4b, which provide heat to the bottom cycle. The mass flow rate in the bottom cycle is only ~1/10 of the total system flow at 100%THA. In addition, the inlet temperature of Heater 4a is only ~350 °C, and the high system pressure leads to a higher CO_2 density than in the other modules. Furthermore, Heater 4a is located in the tail flue region, where the flow area is larger and the velocity is significantly lower. These factors collectively increase the thermal inertia and thereby slow the response of the main steam. It is also noteworthy that, for the same $|\delta_{mCO2}|$, a negative disturbance generally produces a longer t_{sw} than a positive disturbance, especially at large disturbance ratios. This indicates that the thermal re-equilibration process under flow rate reduction is somewhat slower than that under flow rate increases, reflecting the nonlinear dynamic characteristics of the boiler heat transfer process.

In addition to the dynamic responses of the main steam and reheat steam, the wall temperature of each module and the corresponding temperature change rates are also critical indicators for evaluating

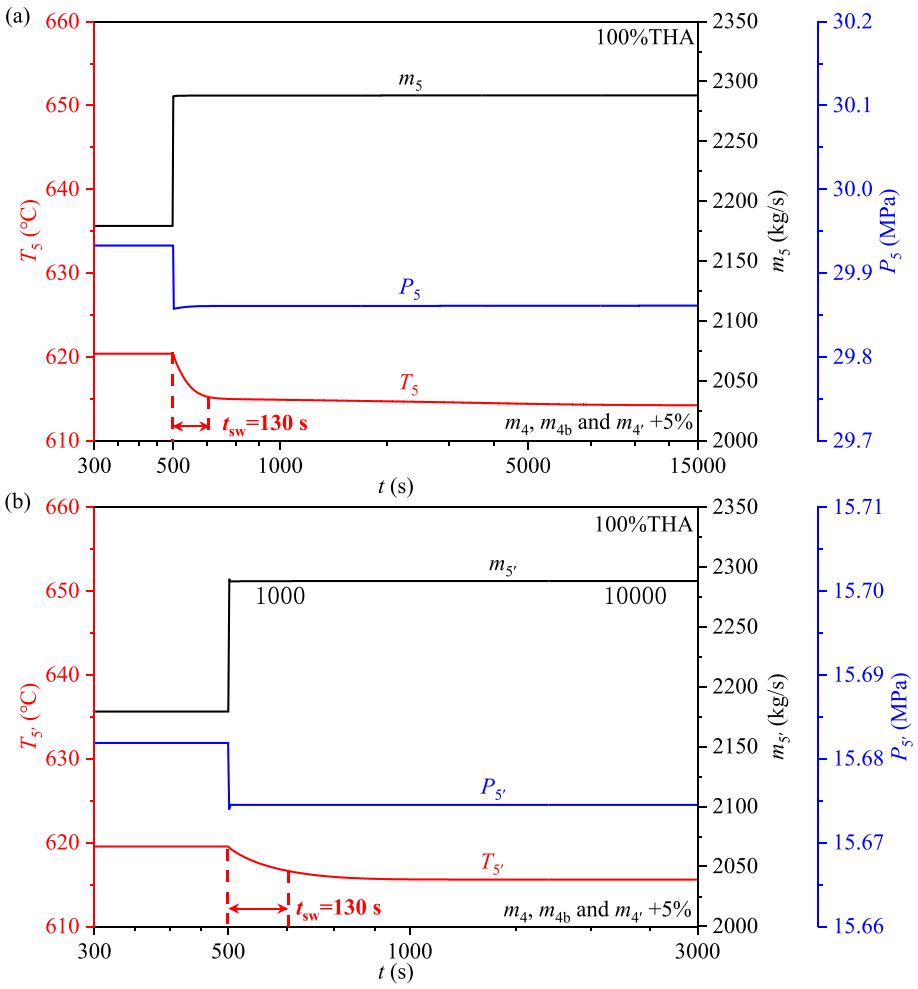


Fig. 7. Variation of temperatures, pressures and mass flow rates of the main steam (a) and reheat steam (b), with +5% stepwise rise of the total CO_2 mass flow rate entering the boiler.

system safety. In the sCO_2 boiler, the materials used in each module have been listed in Table 2. The material temperature limit of Super304H, T91, and 12Cr1MoVG are 705 °C, 650 °C, and 570 °C, respectively. The maximum outer wall temperatures ($T_{wo,max}$) of each module under different δ_{mCO2} at 100%THA are shown in Fig. 9a and b. The red lines correspond to modules made of Super304H, while the black and blue lines represent modules made of T91 and 12Cr1MoVG, respectively.

As illustrated, the $T_{wo,max}$ of each module increases nonlinearly as δ_{mCO2} decreases. Among all modules, Heater 4b exhibits a much steeper increase in $T_{wo,max}$: its $T_{wo,max}$ rises from ~615 °C at $\delta_{mCO2} = +0.25$ to ~735 °C at $\delta_{mCO2} = -0.25$, corresponding to an increase of ~120 °C. By comparison, the variation ranges of other modules are clearly smaller, being ~50-70 °C for Part 1/Part 2, SH1/SH2, HRH1/HRH2 and Heater 4a, and only ~30-40 °C for LRH1/LRH2 over the same disturbance range. This indicates that the wall temperature of Heater 4b is much more sensitive to the reduction in CO_2 flow rate. This can be attributed to its location in the bottom cycle, where the mass flow rate is relatively low, resulting in weaker convective heat transfer. Moreover, Heater 4b is positioned in the cooling wall region exposed to high heat flux, which further amplifies its wall temperature response to δ_{mCO2}. However, Part 1 is the first module to exceed the Super304H temperature limit of 705 °C, at a critical δ_{mCO2} value of ~ −0.15. Therefore, to satisfy the material temperature limit and ensure safe operation, the lower allowable limit of δ_{mCO2} should not be lower than −0.15.

The temperature change rate of tube wall is another important safety indicator. Rapid changes in wall temperature induce internal temperature gradients, which generate thermal stresses and may accumulate into fatigue damage under frequent transients. Restricting the temperature change rate allows sufficient time for heat diffusion and stress relaxation, thereby mitigating thermal stress. This highlights the importance of controlling the wall temperature change rate during transient operations [58]. Accordingly, a limit of 5 K/min [23,32,33], which has been widely adopted in studies of the sCO_2 Brayton cycle, is also used in this study as the safety criterion for evaluating tube wall temperature variation under different disturbance conditions.

Therefore, it is necessary to determine the allowable range of CO_2 flow rate disturbances that keeps the tube wall temperature change rate within the safe range. Fig. 9c shows the maximum tube wall temperature change rates ($\max(dT_w/dt)$) of each module under different δ_{mCO2} at 100%THA. Since the $\max(dT_w/dt)$ of Part 2, SH2, LRH2, and HRH2 exhibit trends similar to those of Part1, SH1, LRH1, and HRH1, only the modules with the higher temperature change rates are selected as representatives. As shown, the $\max(dT_w/dt)$ decreases quasi-linearly with increasing δ_{mCO2}. At $\delta_{mCO2} = -0.2$, Part 1 exhibits the highest $\max(dT_w/dt)$ of ~20.8 K/min, followed by SH1 at 17.0 K/min. Heater 4b and HRH1 remain at an intermediate level of 15.2 and 14.1 K/min, respectively, whereas LRH1 and Heater 4a are much less sensitive, with values of only 4.8 and 0.6 K/min. At $\delta_{mCO2} = +0.2$, the same ranking is generally maintained, but all values become negative, decreasing to about −17.0, −14.9, −13.4, −12.1, −4.4 and −0.6 K/min, respectively. Therefore, among all modules, Part 1 exhibits the highest $\max(dT_w/dt)$ at the same δ_{mCO2}, whereas Heater 4a shows the lowest. The quasi-linear variation of $\max(dT_w/dt)$ with δ_{mCO2} is mainly attributed to the quasi-linear change in CO_2 side heat transfer within the investigated

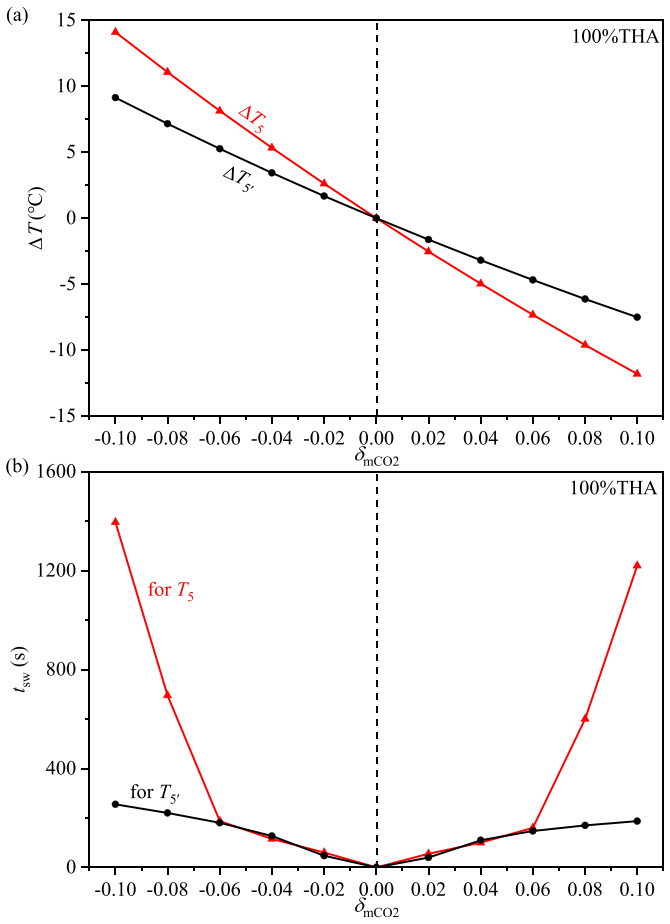


Fig. 8. Variation amplitudes (a) and response times (b) for main steam and reheat steam with respect to disturbance ratio of CO_2 flow rate at the 100% THA condition.

disturbance range. A larger flow rate disturbance causes a larger transient heat imbalance across the tube wall. Since the thermal inertia of the wall remains nearly unchanged, the max(dT_w/dt) also varies approximately linearly with δ_{mCO2}. To determine the safe operating boundary, the disturbance limits are identified from the intersections between the max(dT_w/dt) curves and the ±5 K/min criterion lines. Part 1 is the first module to reach the temperature change rate limit, corresponding to $\delta_{mCO2} = -0.052$ and $\delta_{mCO2} = 0.055$, respectively. Hence, considering the temperature change rate limits of all modules, the allowable range at 100%THA is $-0.052 \leq \delta_{mCO2} \leq 0.055$. It should be noted that, under 100%THA, the wall temperature change rate criterion is more restrictive than the material temperature limit. This indicates that transient thermal safety, rather than the absolute wall temperature, governs the allowable flow rate disturbance under rated condition.

As partial load operation represents an indispensable mode for sCO_2 power systems [50], it is important to determine the allowable CO_2 flow rate disturbance limits under such conditions from the perspective of system safety. Thus, a load-dependent analysis is conducted to evaluate how the disturbance limit varies with load ratio. Fig. 10 illustrates the max(dT_w/dt) of representative modules at 50%THA and 30%THA. It can be observed that max(dT_w/dt) of all modules still decrease approximately linearly with increasing δ_{mCO2}. The ranking of the temperature change rates among the modules remains unchanged. Taking Part 1 as an example, at $\delta_{mCO2} = -0.20$, the max(dT_w/dt) at 50%THA is ~14.8 K/min and further decreases to ~11.4 K/min at 30%THA. As the load ratio decreases, the allowable range of δ_{mCO2} satisfying the 5 K/min limit gradually enlarges: At 50%THA, the critical range is $-0.071 \leq \delta_{mCO2} \leq 0.074$, while at 30%THA it further increases to $-0.091 \leq \delta_{mCO2} \leq 0.096$.

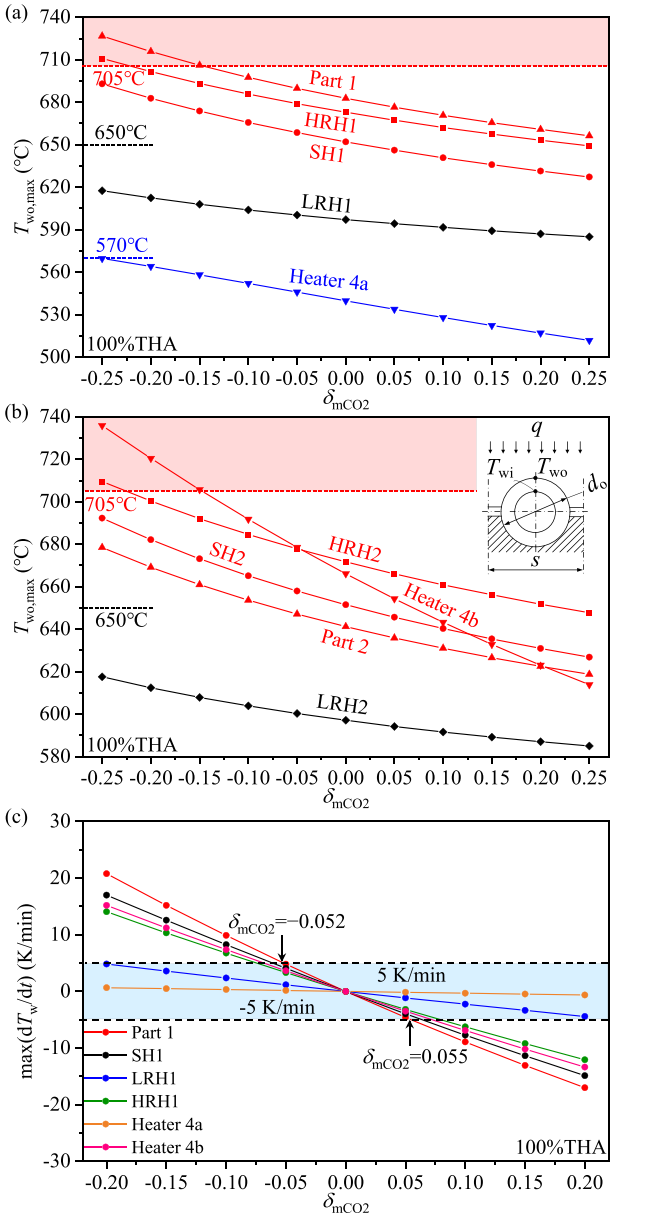


Fig. 9. Maximum outer wall temperatures and temperature change rates of heat transfer modules versus disturbance ratios of CO_2 flow rate at the 100% THA condition. (a) and (b) wall temperatures, (c) wall temperature change rates.

This widening of the safe range is mainly attributed to the lower heat flux and the smaller temperature differences among the flue gas, tube wall, and CO_2 under partial load operation, which weaken the transient heat imbalance induced by the flow rate disturbance. Compared with 100%THA, the safe operating range increases by ~35% at 50%THA and ~75% at 30%THA, demonstrating the significantly improved tolerance of the boiler to flow rate disturbances under partial load conditions.

3.2. *Dynamic characteristics of the boiler under step disturbance of coal feeding rate*

Fig. 11 presents the transient responses of the system following a 5% step increase in coal feeding rate at 500 s. Both the main steam and reheat steam temperatures increase gradually. The main steam temperature rises by 4.0 °C with a response time of ~240 s, while the reheat steam temperature increases by 5.9 °C with a response time of ~210 s.

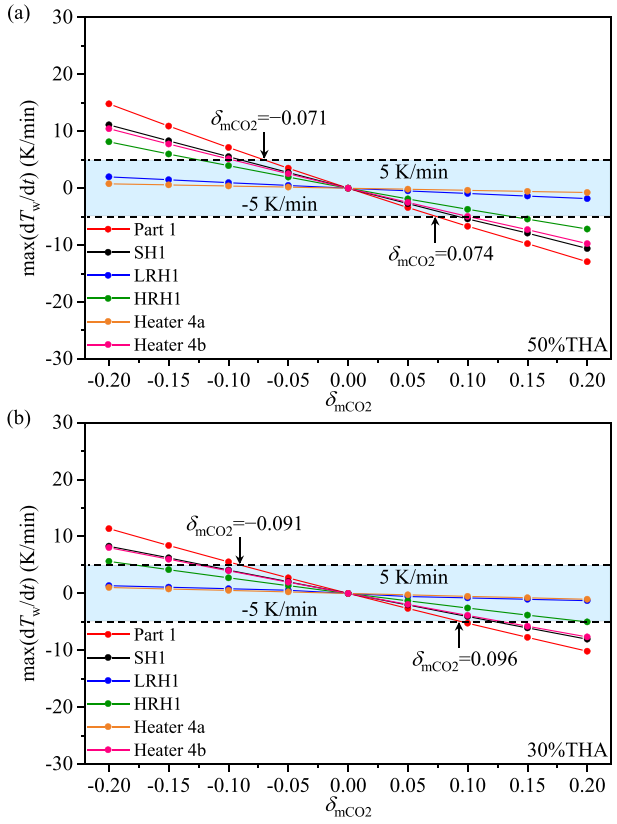


Fig. 10. Wall temperature change rates versus disturbance ratios of CO_2 flow rate under partial load operation, (a) 50%THA condition, (b) 30% THA condition.

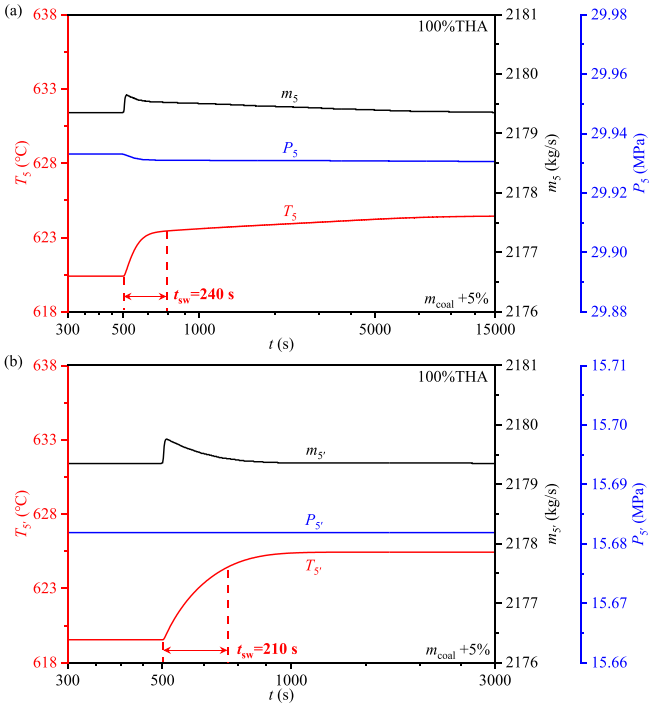


Fig. 11. Variation of temperatures, pressures and mass flow rates of the main steam (a) and reheat steam (b), with +5% stepwise rise of coal feeding rate.

As the temperature increases, the flow velocity rises, leading to higher frictional resistance and a subsequent decrease in main steam pressure. In contrast, the reheat steam pressure remains nearly constant, since the flow velocity in the reheat section is lower and the flow resistance is smaller. The increase in coal input primarily enhances heat transfer to the reheat CO_2 near the boiler outlet. Although the reheat steam temperature rises by 5.9 °C, the average velocity in this section changes only slightly, resulting in negligible pressure drop and thus a stable pressure response. The mass flow rates of both the main steam and reheat steam exhibit an initial increase, followed by a gradual return to their initial values. This behavior can be attributed to the thermal expansion of CO_2 at elevated temperature, which temporarily reduces its density and the total mass stored within the boiler. Consequently, the outlet mass flow rate increases momentarily before returning to equilibrium. When a step disturbance in coal feeding rate is applied to a supercritical water-steam boiler, the outlet temperature exhibits a response trend similar to that of a sCO_2 boiler, accompanied by a brief deviation in outlet mass flow rate [11]. The resulting change in heat absorption alters the mass flow distribution in the heating and evaporation sections. This transient thermophysical imbalance leads to a short fluctuation in mass flow rate before the system reaches a new steady state.

The influence of coal feeding rate disturbance ratio is examined below. As illustrated in Fig. 12a, the temperature variation amplitudes of both the main steam and reheat steam vary approximately linearly with δ_{mcoal}. This behavior is mainly attributed to the fact that, within the investigated disturbance range, a change in coal feeding rate causes an approximately proportional variation in furnace heat release and flue gas enthalpy, which in turn leads to an approximately linear change in the heat transferred to the working fluid. Positive disturbances increase the outlet temperatures, whereas negative disturbances decrease them. For the same δ_{mcoal}, the reheat steam exhibits a larger temperature

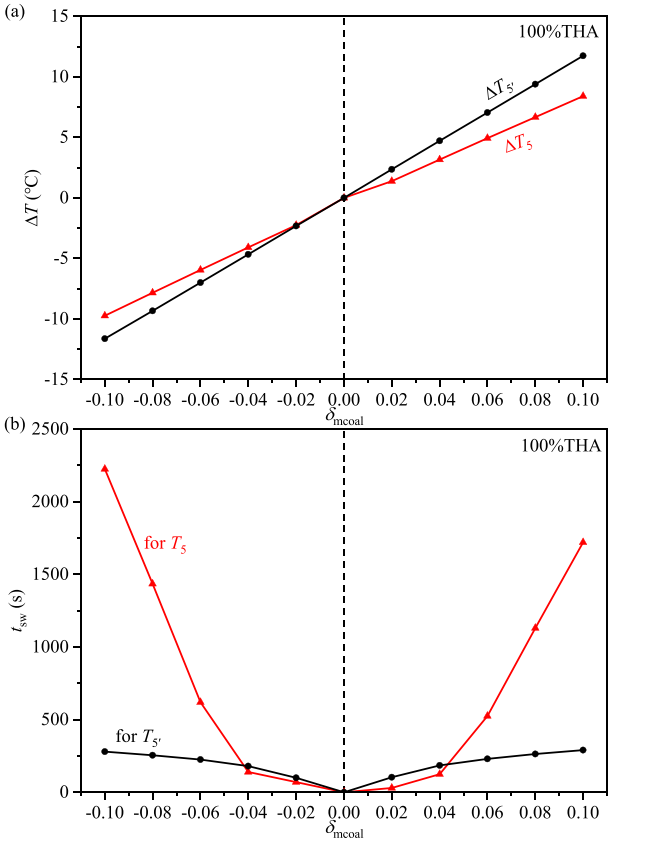


Fig. 12. Variation amplitudes (a) and response times (b) for main steam and reheat steam with respect to disturbance ratios of coal feeding rate at the 100% THA condition.

variation than the main steam. A +10% step increase in coal feeding rate results in temperature rises of 8.4 °C and 11.7 °C for the main and reheat steam, respectively, while a −10% decrease leads to corresponding temperature drops of −9.7 °C and −11.6 °C. These results demonstrate that the reheat steam is more sensitive to variations in coal feeding rate. In addition, a slight asymmetry is observed in the main steam response: the temperature drops under a −10% disturbance is ~1.3 °C larger than the temperature rise under a +10% disturbance, whereas the reheat steam shows an almost symmetric response, with a difference of only 0.1 °C.

Fig. 12b illustrates that both T_5 and $T_{5'}$ increase with $|\delta_{mcoal}|$, although their sensitivities differ markedly. For T_5, t_{sw} rises sharply in both the positive and negative directions and shows an approximately exponential growth trend. t_{sw} is only ~140 s and 125 s at $\delta_{mcoal} = -0.04$ and + 0.04, respectively, but increases rapidly to ~2230 s at −0.10 and 1720 s at +0.10. In contrast, the response of $T_{5'}$ is much milder and follows an approximately parabolic trend, with t_{sw} increasing from ~190 s at $|\delta_{mcoal}| = 0.04$ to only ~290 s at $|\delta_{mcoal}| = 0.10$, respectively. Overall, the main steam system demonstrates greater thermal inertia, which leads to a slower stabilization process to coal disturbance. The reheat system exhibits a faster response and enhanced dynamic adaptability. Compared with CO_2 flow rate disturbances, coal feeding rate disturbances produce a smaller temperature variation amplitude but a much longer response time for the main steam, while for the reheat steam they produce a larger variation amplitude and a slightly longer response time.

As shown in Fig. 13a and b, $T_{wo,max}$ of all modules increase quasi-linearly with δ_{mcoal}. This behavior is mainly attributed to the fact that an increase in coal feeding rate causes an almost proportional rise in furnace heat release and flue gas temperature, thereby increasing the local heat flux absorbed by each heating surface and leading to a nearly linear increase in wall temperature. Among all modules, Heater 4b shows the strongest sensitivity. By comparison, the variation ranges of the other modules are clearly smaller, being ~40-60 °C for Part 1/Part 2, SH1/SH2 and LRH1/LRH2, and ~70-90 °C for HRH1/HRH2 and Heater 4a over the same disturbance range, whereas Heater 4b exhibits the largest increase of ~130 °C. This is mainly attributed to the relatively low CO_2 flow rate in the bottom cycle and the location of Heater 4b in the cooling wall region with high heat flux, where weaker convective cooling makes the wall temperature more sensitive to variations in furnace heat input. Consequently, Heater 4b is the first module to exceed its material temperature limit of 705 °C. Specifically, the wall temperature of Heater 4b rises from ~666 °C at $\delta_{mcoal} = 0$ to ~714 °C $\delta_{mcoal} = +0.2$, crossing the safety limit at a critical disturbance ratio of ~0.16. Therefore, from the perspective of material temperature limit, the δ_{mcoal} should be restricted to below 0.16.

Fig. 13c presents the variation of $\max(dT_w/dt)$ with δ_{mcoal} at 100% THA. The results indicate that $\max(dT_w/dt)$ for all modules increase quasi-linearly with increasing δ_{mcoal}. Specifically, when $\delta_{mcoal} = -0.20$, $\max(dT_w/dt)$ ranges from only ~–1.4 K/min in Heater 4a to ~ –17.0 K/min in HRH1; Part 1 and SH1 also show relatively large values of ~ –15.9 K/min and −12.1 K/min, whereas Heater 4b and LRH1 remain at intermediate levels of ~ –11.0 K/min and −7.3 K/min, respectively. When $\delta_{mcoal} = +0.20$, the same trend is maintained, with the values increasing to ~14.5, 14.0, 10.6, 9.1, 7.4 and 1.7 K/min for HRH1, Part 1, SH1, Heater 4b, LRH1, and Heater 4a, respectively. Therefore, at the same δ_{mcoal}, the HRH1 exhibits the highest $|\max(dT_w/dt)|$, whereas the Heater 4a shows the lowest. The stronger response of HRH1 may be attributed to its closer thermal coupling with the high temperature flue gas, making its wall temperature more sensitive to combustion side heat input variations, whereas Heater 4a is located in a relatively low temperature region and therefore shows the smallest temperature change rate. The quasi-linear behavior is mainly attributed to the fact that, within the investigated disturbance range, the coal feeding rate causes an approximately proportional change in heat release, while the thermal inertia of the tube wall remains nearly unchanged. As a result, the

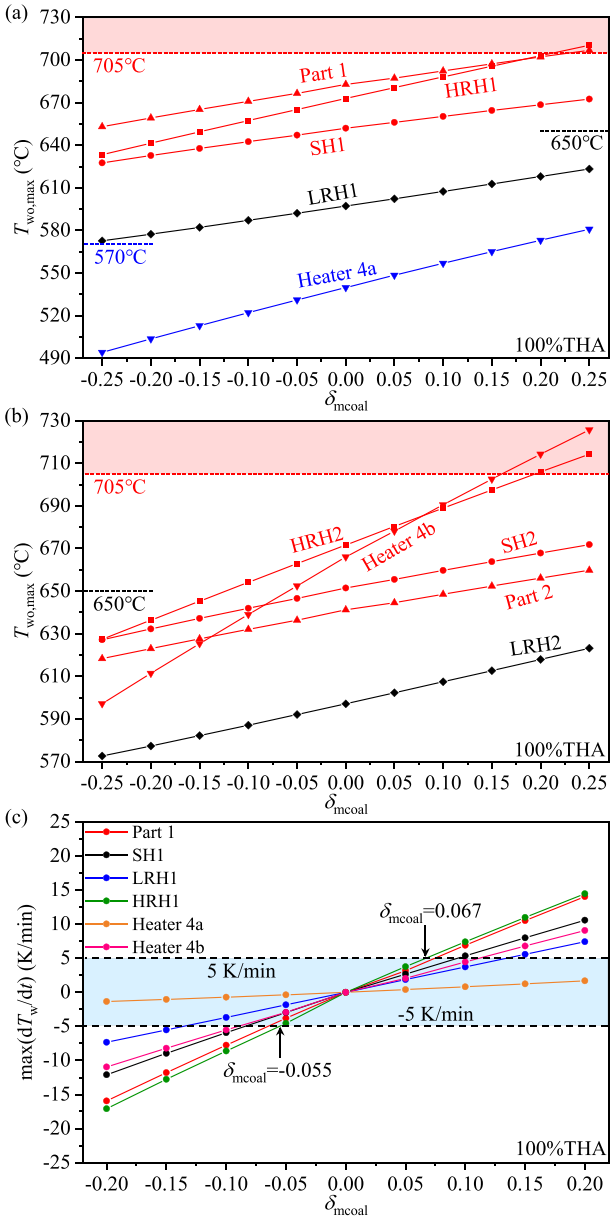


Fig. 13. Maximum outer wall temperatures and temperature change rates of heat transfer modules versus different δ_{mcoal} at the 100%THA condition, (a) and (b) wall temperatures, (c) wall temperature change rates.

transient heat imbalance at the wall varies almost linearly with δ_{mcoal}, leading to a nearly linear change in temperature change rate. Based on the criterion of temperature change rate, the allowable limits of coal feeding rate disturbances can be determined. When $\delta_{mcoal} = -0.055$ and $\delta_{mcoal} = 0.067$, the system reaches its critical condition. Therefore, considering the safety of all modules, the allowable range of coal feeding disturbances at 100%THA should be maintained within $-0.055 \leq \delta_{mcoal} \leq 0.067$. It should be noted that the wall temperature change rate criterion is also more restrictive than the material temperature limit under 100%THA.

As shown in Fig. 14, $\max(dT_w/dt)$ of all representative modules still increases quasi-linearly with δ_{mcoal} at both 50% and 30%THA. At the same $|\delta_{mcoal}|$, HRH1 and Part 1 exhibit the largest wall temperature change rates and remain very close to each other, whereas Heater 4a shows the weakest response. Specifically, at $\delta_{mcoal} = -0.2$, the max (dT_w/dt) at 50%THA are about −11.9, −11.5, −8.2, −7.6, −3.6 and −0.6 K/min for HRH1, Part 1, SH1, Heater 4b, LRH1, and Heater 4a,

respectively, and they further decrease to about −9.2, −8.9, −6.1, −5.9, −2.1 and −0.6 K/min at 30% THA. Correspondingly, the allowable disturbance range defined by the ±5 K/min limit expands from $-0.086 \le \delta_{mcoal} \le 0.091$ at 50%THA to $-0.112 \le \delta_{mcoal} \le 0.117$ at 30%THA. This widening of the safe range is mainly attributed to the reduction in furnace heat release and in the temperature differences among the flue gas, tube wall, and working fluid under lower load operation, which weakens the transient heat imbalance caused by the coal disturbance. As a result, the wall temperature response becomes milder and $\max(dT_w/dt)$ decreases. In addition, the allowable coal disturbance ratios are slightly larger than those for the CO_2 flow rate disturbance.

The previous analysis examined the allowable disturbance ratios of CO_2 flow rate and coal feeding rate at 50%THA and 30%THA. To further clarify the effect of load ratios on system tolerance to disturbances, Fig. 15 presents the allowable disturbance ratios of CO_2 flow rate and coal feeding rate over the operating range from 30% to 100%THA. Under a positive disturbance in the CO_2 flow rate (see Fig. 15a), the upper disturbance ratio limit, $\delta_{mCO2,max}$, gradually increases as the load ratio decreases. Specifically, $\delta_{mCO2,max}$ is ~0.06 at 100%THA and increases to ~0.10 at 30%THA. However, the corresponding disturbance amplitude limit, $\varphi_{mCO2,max}$, exhibits a parabolic trend: it first decreases, reaching its minimum around 70%THA, and then increases as load continues to decline. A similar trend is observed for a negative disturbance in the CO_2 flow rate (see Fig. 15b), where $|\delta_{mCO2,max}|$ also increases as the load ratio decreases. Likewise, $|\varphi_{mCO2,max}|$ follows a parabolic trend, with its minimum occurring near 60%THA. Overall, as the load decreases, the allowable disturbance ratios of CO_2 flow rate increase steadily, while the corresponding disturbance amplitude limit shows a nonlinear dependence on load ratio.

When the coal feeding rate experiences a positive disturbance (see Fig. 15c), the upper disturbance ratio limit, $\delta_{mcoal,max}$, also gradually increases as the load ratio decreases: rising from ~0.07 at 100%THA to ~0.12 at 30%THA. Correspondingly, the disturbance amplitude limit, $\varphi_{mcoal,max}$, decreases monotonically with the decreasing load ratio, reflecting the higher baseline coal input at higher loads. Similarly, for negative disturbances (see Fig. 15d), $|\delta_{mcoal,max}|$ also increases as the load ratio decreases, whereas $|\varphi_{mcoal,max}|$ shows a consistent monotonic decrease. These results indicate that, as the load decreases, the system becomes more tolerant to disturbance ratios of the coal feeding rate, while the disturbance amplitude limit becomes smaller.

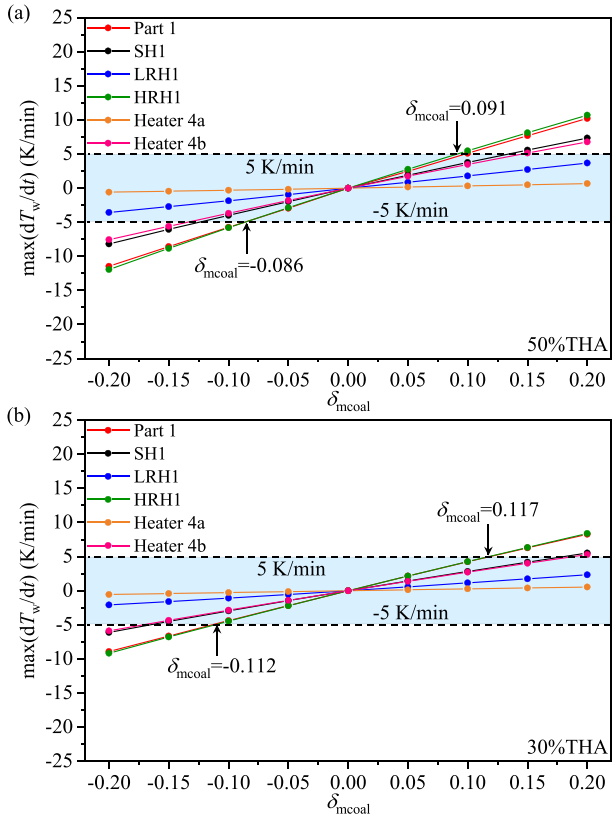


Fig. 14. Wall temperature change rates versus disturbance ratios of coal feeding rate under partial load operation, (a) 50%THA condition, (b) 30% THA condition.

The dynamic response of heating surfaces subjected to disturbances can be effectively approximated using a transfer-function model: $W(s) = \frac{K_g}{(1+Ts)^n}$, where K_g represents the steady-state gain, describing the degree to which the system amplifies or attenuates an input disturbance. The time constant (T) governs the response speed, indicating how rapidly the heating surface reacts to disturbance. The order (n) reflects the number of inertial stages, and thus captures the complexity of energy transfer pathways and the coupling strength of thermal-hydraulic interactions [59,60]. The response time of the heating surface, t_{sw}, is therefore mainly determined by the combined influence of T and n.

Both parameters are governed by three fundamental quantities: the flow time (τ_0), the metal thermal storage time constant (τ_m), and dynamic parameter (β): $\tau_0 = L/v$, $\tau_m = G_m c_m/(\alpha_f A_t)$, $\beta = \alpha_f A_t/(mc_f)$ [60]. Here, L denotes the length of the heating surface, v is the working fluid velocity, G_m is the metal mass of the tube, c_m is the metal specific heat, α_f is the inner wall heat transfer coefficient, A_t is the total internal surface area of the tube, m is the mass flow rate of working fluid, and c_f is its specific heat. Hence, the response time is jointly determined by the fluid side heat transfer characteristics and the thermal inertia of the metal wall, both of which govern the overall transient behavior of the heating surface.

Fig. 16 compares the response times predicted by the transfer-function model with those obtained from numerically simulations for four representative heating modules (Part 1, SH1, LRH1 and HRH1), each subjected independently to a 5% step increase in CO_2 flow rate. SH1 has the shortest response time of approximately 1 min, while LRH1 has the longest response time of about 8 min. The close agreement between the two sets of results confirms that the transfer-function provides a reliable and robust representation of the transient thermodynamic behavior of the modules. Based on the above analysis, the key strategies to enhance boiler flexibility include: (i) reducing the flow time through optimized module arrangement; (ii) lowering metal thermal storage by employing thinner tubes or materials with higher thermal conductivity in high heat flux regions; (iii) enhancing local heat transfer selectively in modules with slow responses; (iv) improving control coordination to mitigate temperature overshoot during rapid load transitions. These findings provide valuable guidance for the development of control systems for the CO_2 boiler.

Previous dynamic studies on conventional water-steam boilers mainly focused on outlet temperature response [24,26], flow instability [28], and the thermo-mechanical behavior of water-cooled walls under feedwater or heat load disturbances [25], as well as under low load peak shaving conditions [28]. However, they were still mainly limited to water-cooled walls or steam temperature control in water-steam systems. Current studies on the dynamic characteristics of sCO_2 boilers mainly focus on the responses of working fluid side parameters [22] and on the transient temperature variation of the cooling wall during load change processes [23]. In contrast, the present study extends the analysis to an entire coal-fired sCO_2 boiler and establishes a more complete disturbance safety framework. This study quantitatively determines the allowable disturbance ranges of both CO_2 flow rate and coal feeding rate at different load ratios from 30% to 100%THA by considering two wall side safety constraints, namely the material temperature limit and the wall temperature change rate. Therefore, the significance of the present work lies in identifying load-dependent disturbance boundaries for all major heating modules in the sCO_2 boiler, which provides a more direct

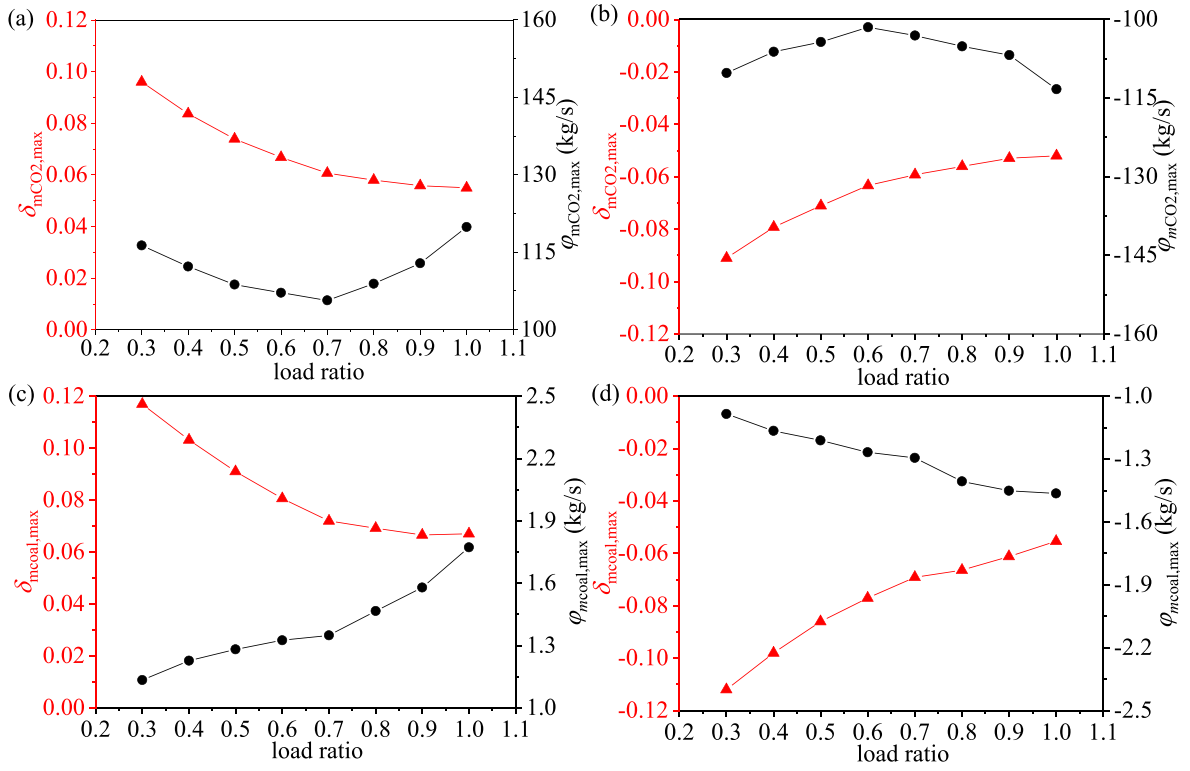


Fig. 15. Allowable disturbance ratios of CO_2 flow rate and coal feeding rate, (a) positive deviation of CO_2 flow rate, (b) negative deviation of CO_2 flow rate, (c) positive deviation of coal feeding rate, (d) negative deviation of coal feeding rate.

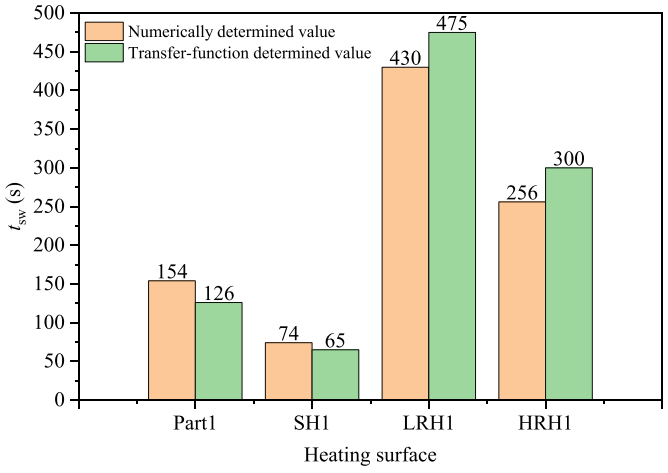


Fig. 16. Comparison of response time between numerically determined values and transfer-function determined values.

basis for safe and flexible operation than the response only or single indicator analyses commonly reported in earlier studies.

Future work should focus on establishing a more comprehensive dynamic model of the sCO_2 coal-fired power generation system to further explore the influence of various parameter disturbances on its operating characteristics. Furthermore, it is necessary to develop an experimental platform for model validation, which would provide reliable data support for enhancing model credibility. Future research should also address the integration of control strategies, system-level dynamic coupling, so as to provide stronger theoretical and practical support for safe and flexible operation of sCO_2 coal-fired power generation systems.

4. Conclusion

The sCO_2 boiler is a key component to couple with the cycle. Transient simulation under disturbances of CO_2 flow rate and coal feeding rate was performed, focusing on the allowable disturbance ratios to keep not only the material temperature limit, but also the temperature change rate limit. Conclusions are summarized as follows.

1. Variational amplitudes of main steam (ΔT_5) and reheat steam ($\Delta T_{5'}$) show quasi-linear change versus disturbance ratios of CO_2 flow rate (δ_{mCO2}). The curve of response time is approximatively symmetrically populated against the zero-deviation line, with δ_{mCO2} in the range from −10% to 10%.
2. Negative disturbance of CO_2 flow rate increases wall temperatures. The 705 °C temperature limit yields a 15% allowable disturbance ratio of CO_2 flow rate at the base load of 100%THA. The 5 K/min change rate limit yields a −5.2% negative and 5.5% positive allowable disturbance ratios of CO_2 flow rate, concluding stricter criterion than the material temperature limit.
3. Partial load operation obviously enlarges allowable disturbance ratios of CO_2 flow rate, which is (9~10)% at the 30%THA, 1.75 times of (5~6)% at the 100%THA, concluding safer operation under partial load condition than the rated condition.
4. Transient outcomes with disturbance of coal feeding rate are similar to those with disturbance of CO_2 flow rate. Compared with CO_2 flow rate disturbance, coal disturbance yields smaller variation amplitude on main steam but larger variation amplitude on reheat steam, and yields longer response times for both main and reheat steam.
5. Allowable coal disturbance ratio is (5~7)% and (11~12)% at the 100%THA condition and the 30%THA condition, respectively, which are slightly larger than those for the CO_2 flow rate disturbance.
6. Under a 5% increase disturbance of CO_2 flow rate applied independently to heating surfaces, the response time covers a range from 1 to 8 min. The numerically simulated values match the transfer-function

determined values well, which are helpful to develop the sensor and control system for the CO_2 boiler.

7. Future work should focus on developing a complete dynamic model of the sCO_2 coal-fired power generation system to further explore the effects of different parameter disturbances on its operating characteristics.

Nomenclature

A	area, m^2	λ	thermal conductivity, W/(m·K)
B	coal feeding rate, kg/s	η	efficiency
c	specific heat capacity, kJ/(kg·K)	γ	non-uniformity coefficient of heat flux in furnace height direction
C_s	correction coefficient for tube bundle geometric arrangement	ρ	density, kg/m^3
C_z	correction coefficient for the number of tube rows along the flue gas flow direction	ϕ	heat retention coefficient
d	diameter, mm	τ_0	characteristic time for fluid flow
f	friction coefficient	τ_m	characteristic time for thermal storage of metal wall
g	gravity acceleration, m/s^2	μ	dynamic viscosity, Pa·s
G	mass flux, $kg/(m^2 \cdot s)$		
h	enthalpy, kJ/kg	*Subscripts*	
$h_{fg,o}$	enthalpy of flue gas at furnace outlet, kJ/kg	ar	as received basis
H	height, m	ave	average
K	non-dimensional parameter representing evaporation induced momentum force relative to inertia force	b	boiler
K_g	steady-state gain	c	cross-section
L	length, m	d	disturbance
m	mass flow rate, kg/s	daf	dry ash-free basis
n	order of the transfer-function model	f	fluid
Nu	Nusselt number	fg	flue gas
P	pressure, MPa	i	inner
P_f	friction pressure drop, MPa	lim	limit
Pr	Prandtl number	m	metal
q	heat flux, kW/m^2; heat loss percentage of boiler	min	minimum
Q_a	thermal input from preheated air, kJ/kg	max	maximum
Q_f	heat source term, kW/m^3	o	outer
Q_{fg}	heat source term of heat released by flue gas, kW/m^3	sw	response
Q_{ef}	effective heat input, kJ/kg	t	total
Q_{LHV}	lower heating value of coal, kJ/kg	w	wall
r	radius, mm	wi	inner wall
Re	Reynolds number	wo	outer wall
s	tube pitch, mm		
t	time, s	*Abbreviations*	
t_d	disturbance starting time, s	ACM	Aspen Custom Modeler
t_{sw}	response time, s	C1	main compressor
T	temperature, °C; time constant	C2	auxiliary compressor
T_5	main steam temperature, °C	CFPP	coal-fired power plant
$T_{5'}$	reheat steam temperature, °C	EAP	external air preheater
v	velocity, m/s	HRH	high temperature reheater
z	axial coordinate	HTR	high temperature recuperator
		LRH	low temperature reheater
Greek symbols		LTR	low temperature recuperator
α	heat transfer coefficient, $W/(m^2 \bullet K)$	RC	recompression cycle
β	dynamic parameter	RH	reheating
δ	disturbance ratio	sCO_2	supercritical carbon dioxide

(*continued on next column*)

(*continued*)

δ_{mCO2}	disturbance ratio of CO_2 flow rate	SH	superheater
δ_{mcoal}	disturbance ratio of coal feeding rate	T1	high pressure turbine
Δ	absolute roughness of internal tube wall, mm	T2	low pressure turbine
ΔT_5	variation amplitude of main steam temperature, °C	THA	turbine heat acceptance
$\Delta T_{5'}$	variation amplitude of reheat steam temperature, °C		
σ	disturbed variable		
σ_s	initial value of disturbed variable		
φ	disturbance amplitude		

CRediT authorship contribution statement

Binghan Ma: Writing – original draft, Software, Methodology, Investigation, Formal analysis. **Jinliang Xu:** Writing – review & editing, Methodology, Funding acquisition, Conceptualization. **Bin Shen:** Writing – review & editing, Methodology. **Chuxiong Wang:** Writing – review & editing, Validation. **Guanglin Liu:** Writing – review & editing, Validation.

Declaration of competing interest

We state that the manuscript titled as " Allowable disturbance ratios of CO_2 flow rate and coal feeding rate for coal-fired supercritical carbon dioxide boiler " by Binghan Ma, Jinliang Xu, Bin Shen, Chuxiong Wang, Guanglin Liu does not have any conflict of interest including any financial, personal or other relationships with other people or organizations within three years of beginning the submitted work that could inappropriately influence, or be perceived to influence, the present work.

Acknowledgements

This work was supported by the Natural Science Foundation of China (52130608).

Data availability

Data will be made available on request.

References

[1] Geng W, Ming Z, Lilin P, Ximei L, Bo L, Jinhui D. China's new energy development: status, constraints and reforms. Renew Sustain Energy Rev 2016;53:885–96. https://doi.org/10.1016/j.rser.2015.09.054.

[2] Wang J, Xiao Y, Yu Q, Zhang C. HSD17B1 could serve as a prognostic biomarker for urinary bladder patients. Asian J Surg 2023;46:5379–81. https://doi.org/10.1016/j.asjsur.2023.07.088.

[3] Notton G, Nivet ML, Voyant C, Paoli C, Darras C, Motte F, et al. Intermittent and stochastic character of renewable energy sources: consequences, cost of intermittence and benefit of forecasting. Renew Sustain Energy Rev 2018;87:96–105. https://doi.org/10.1016/j.rser.2018.02.007.

[4] Uddin M, Romlie MF, Abdullah MF, Abd Halim S, Abu Bakar AH, Chia Kwang T. A review on peak load shaving strategies. Renew Sustain Energy Rev 2018;82:3323–32. https://doi.org/10.1016/j.rser.2017.10.056.

[5] Gonzalez-Salazar MA, Kirsten T, Prchlik L. Review of the operational flexibility and emissions of gas- and coal-fired power plants in a future with growing renewables. Renew Sustain Energy Rev 2018;82:1497–513. https://doi.org/10.1016/j.rser.2017.05.278.

[6] Merzic A, Music M, Haznadar Z. Conceptualizing sustainable development of conventional power systems in developing countries – a contribution towards low carbon future. Energy 2017;126:112–23. https://doi.org/10.1016/j.energy.2017.03.016.

[7] Zhao Y, Liu M, Wang C, Li X, Chong D, Yan J. Increasing operational flexibility of supercritical coal-fired power plants by regulating thermal system configuration during transient processes. Appl Energy 2018;228:2375–86. https://doi.org/10.1016/j.apenergy.2018.07.070.

[8] Hentschel J, Babić U, Spliethoff H. A parametric approach for the valuation of power plant flexibility options. Energy Rep 2016;2:40–7. https://doi.org/10.1016/j.egyr.2016.03.002.
[9] Richter M, Oeljeklaus G, Görner K. Improving the load flexibility of coal-fired power plants by the integration of a thermal energy storage. Appl Energy 2019;236:607–21. https://doi.org/10.1016/j.apenergy.2018.11.099.
[10] Liu JZ, Yan S, Zeng DL, Hu Y, Lv Y. A dynamic model used for controller design of a coal fired once-through boiler-turbine unit. Energy 2015;93:2069–78. https://doi.org/10.1016/j.energy.2015.10.077.
[11] Liu K, Wang C, Wang L, Liu B, Ye M, Guo Y, et al. Dynamic performance analysis and control strategy optimization for supercritical coal-fired boiler: a dynamic simulation. Energy 2023;282. https://doi.org/10.1016/j.energy.2023.128712.
[12] Yang Y, Chem H, Hao J, Yang Z, Xu G, Duan L. Development pathways for the transformation and upgrading of China's coal-fired power generation under the goals of carbon peak and carbon neutrality. Proc CSEE 2024;44:6900–8.
[13] Huang C, Li Z, Lu Y, Chen Z, Liu H, Kang Y, et al. Research on a novel universal low–load stable combustion technology. Energy 2024;310. https://doi.org/10.1016/j.energy.2024.133223.
[14] Zhao Y, Fan P, Wang C, Liu M, Chong D, Yan J. Fatigue lifetime assessment on a high-pressure heater in supercritical coal-fired power plants during transient processes of operational flexibility regulation. Appl Therm Eng 2019;156:196–208. https://doi.org/10.1016/j.applthermaleng.2019.04.066.
[15] Cruz MRM, Fitiwi DZ, Santos SF, Catalão JPS. A comprehensive survey of flexibility options for supporting the low-carbon energy future. Renew Sustain Energy Rev 2018;97:338–53. https://doi.org/10.1016/j.rser.2018.08.028.
[16] Liu C, Xu J, Li M, Wang Z, Xu Z, Xie J. Scale law of sCO2 coal fired power plants regarding system performance dependent on power capacities. Energy Convers Manag 2020;226. https://doi.org/10.1016/j.enconman.2020.113505.
[17] Xu J, Sun E, Li M, Liu H, Zhu B. Key issues and solution strategies for supercritical carbon dioxide coal fired power plant. Energy 2018;157:227–46. https://doi.org/10.1016/j.energy.2018.05.162.
[18] Sun E, Xu J, Li M, Liu G, Zhu B. Connected-top-bottom-cycle to cascade utilize flue gas heat for supercritical carbon dioxide coal fired power plant. Energy Convers Manag 2018;172:138–54. https://doi.org/10.1016/j.enconman.2018.07.017.
[19] Sun E, Xu J, Hu H, Li M, Miao Z, Yang Y, et al. Overlap energy utilization reaches maximum efficiency for S-CO2 coal fired power plant: a new principle. Energy Convers Manag 2019;195:99–113. https://doi.org/10.1016/j.enconman.2019.05.009.
[20] Zhu B, Xu J, Wu X, Xie J, Li M. Supercritical "boiling" number, a new parameter to distinguish two regimes of carbon dioxide heat transfer in tubes. Int J Therm Sci 2019;136:254–66. https://doi.org/10.1016/j.ijthermalsci.2018.10.032.
[21] Liu C, Xu J, Li M, Wang Q, Liu G. The comprehensive solution to decrease cooling wall temperatures of sCO2 boiler for coal fired power plant. Energy 2022;252. https://doi.org/10.1016/j.energy.2022.124021.
[22] Liu K, Wang L, Bai W, Che D. Comparative study on dynamic characteristics of 600 MW supercritical coal-fired boilers using CO2 and water as working fluids. Energy 2025;314. https://doi.org/10.1016/j.energy.2024.134296.
[23] Ma B, Xu J, Zheng H, Wang T, Xie J. Transient cooling wall temperatures of supercritical carbon dioxide boiler during load variation process. Energy 2025;336. https://doi.org/10.1016/j.energy.2025.138365.
[24] Kim S, Choi S. Dynamic simulation of the water-steam flow in a supercritical once-through boiler. J Mech Sci Technol 2017;31:4965–75. https://doi.org/10.1007/s12206-017-0945-z.
[25] Wang C, Chen X, Liu B, Liu K, Han Y, Wang L, et al. Dynamic analysis for ultra-supercritical boiler water wall considering uneven heat flux distribution and combustion instability. Int J Heat Mass Transf 2025;236. https://doi.org/10.1016/j.ijheatmasstransfer.2024.126269.
[26] Zhu H, Tan P, He Z, Ma L, Zhang C, Fang Q, et al. Revealing steam temperature characteristics for a double-reheat unit under coal calorific value variation. Energy 2023;283. https://doi.org/10.1016/j.energy.2023.128530.
[27] Guo MM, Hao Y, Nižetić S, Lee KY, Sun L. Modelica-based heating surface modelling and dynamic exergy analysis of 300 MW power plant boiler. Energy Convers Manag 2024;312. https://doi.org/10.1016/j.enconman.2024.118557.
[28] Tao Q, Lei X, Hu Y, Zhou X. Flow instability of 600 MW supercritical boiler water-cooled wall under low-load in deep peak-shaving process. Energy 2025;333. https://doi.org/10.1016/j.energy.2025.137517.
[29] Li B, Gao J, Wang C, Han H, Wang X, Li S. Fluid-Structure interaction analysis of a 1000 MW supercritical coal-fired boiler water-cooled wall based on Multi-parameter simulation. Appl Therm Eng 2025;274. https://doi.org/10.1016/j.applthermaleng.2025.126668.
[30] Kumar S, Kumar M, Handa A. Combating hot corrosion of boiler tubes – a study. Eng Fail Anal 2018;94:379–95. https://doi.org/10.1016/j.engfailanal.2018.08.004.
[31] Alshahrani AM, Lim CH, Kim J, Zhang Y. Transient thermal stresses developed during speed sintering of 3 mol% yttria-stabilized tetragonal zirconia polycrystals. Dent Mater 2023;39:522–8. https://doi.org/10.1016/j.dental.2023.04.004.
[32] Li X, Qin Z, Dong K, Wang L, Lin Z. Experimental study of the startup of a supercritical CO2 recompression power system. Energy 2023;284. https://doi.org/10.1016/j.energy.2023.128538.
[33] Liu K, Guo Y, Wang L, Fan G, Che D. Control of supercritical CO2 Brayton cycle for fast and efficient load variation processes. Appl Therm Eng 2024;244. https://doi.org/10.1016/j.applthermaleng.2024.122797.
[34] Dong YANG, Jie PAN. Experimental Study and theoretical calculation on hydrodynamic characteristics of (Ultra) supercritical boiler. Beijing: China Electric Power Press; 2017.
[35] Hedrick K, Hedrick E, Omell B, Zitney SE, Bhattacharyya D. Dynamic modeling, parameter estimation, and data reconciliation of a supercritical pulverized coal-fired boiler. Ind Eng Chem Res 2022;61:16764–79. https://doi.org/10.1021/acs.iecr.2c01977.
[36] Wang D, Jing H, Yuan Z, Zhao Y, Chen W, Wang C, et al. Quantitative prediction of overheating risk at the dry-out point for the cooling wall during dynamic processes considering uneven heat flux distribution and flow deviation. Int J Heat Mass Transf 2025;251. https://doi.org/10.1016/j.ijheatmasstransfer.2025.127423.
[37] Alobaid F, Mertens N, Starkloff R, Lanz T, Heinze C, Epple B. Progress in dynamic simulation of thermal power plants. Prog Energy Combust Sci 2017;59:79–162. https://doi.org/10.1016/j.pecs.2016.11.001.
[38] Brown GO. Environmental and Water Resources History the History of the Darcy-weisbach equation for pipe flow resistance. n.d.
[39] Wang Z, Sun B, Wang J, Hou L. Experimental study on the friction coefficient of supercritical carbon dioxide in pipes. Int J Greenh Gas Control 2014;25:151–61. https://doi.org/10.1016/j.ijggc.2014.04.014.
[40] Seamless stainless steel tubes for boiler and heat exchanger. National standards of P.R.C, GB; 2013.
[41] Li F, Bai B. A model of heat transfer coefficient for supercritical water considering the effect of heat transfer deterioration. Int J Heat Mass Transf 2019;133:316–29. https://doi.org/10.1016/j.ijheatmasstransfer.2018.12.121.
[42] Zhu B, Xu J, Yan C, Xie J. The general supercritical heat transfer correlation for vertical up-flow tubes: k number correlation. Int J Heat Mass Transf 2020;148. https://doi.org/10.1016/j.ijheatmasstransfer.2019.119080.
[43] Bishop AA, Sandberg RO, Tong L. Forced convection heat transfer to water at near-critical temperatures and super-critical pressures. 1964. Pittsburgh, PA, USA.
[44] Jackson JD. Fluid flow and convective heat transfer to fluids at supercritical pressure. Nucl Eng Des 2013;264:24–40. https://doi.org/10.1016/j.nucengdes.2012.09.040.
[45] Jackson JD, Hall WB. Influences of buoyancy on heat transfer to fluids flowing in vertical tubes under turbulent conditions. Turbulent Forced Convection in Channels and Bundles 1979:613–40.
[46] Yu J, Jia B, Wu D, Wang D. Optimization of heat transfer coefficient correlation at supercritical pressure using genetic algorithms. Heat and Mass Transfer/Waerme-Und Stoffuebertragung 2009;45:757–66. https://doi.org/10.1007/s00231-008-0475-4.
[47] Gupta S, Saltanov E, Mokry SJ, Pioro I, Trevani L, McGillivray D. Developing empirical heat-transfer correlations for supercritical CO 2 flowing in vertical bare tubes. Nucl Eng Des 2013;261:116–31. https://doi.org/10.1016/j.nucengdes.2013.02.048.
[48] Teplovoy raschet kotlov (Normativnyi metod). third ed. Saint Petersburg: NPO CKTI; 1998.
[49] Bai W, Zhang Y, Yang Y, Li H, Yao M. 300 MW boiler design study for coal-fired supercritical CO2 Brayton cycle. Appl Therm Eng 2018;135:66–73. https://doi.org/10.1016/j.applthermaleng.2018.01.110.
[50] Zheng H, Miao Z, Xu J. Partial load operation characteristics of supercritical CO2 coal-fired power generation system. Energy 2024;291. https://doi.org/10.1016/j.energy.2024.130415.
[51] Qiao Y, Wang S, Bai W, Zhang Y, Zhang X, Li H, et al. Modeling and dynamic characteristic analysis for boiler in 5 MW supercritical carbon dioxide cycle power unit. Therm Power Gener 2024;53:39–48.
[52] Che D, Zhuang Z, Li J. Boiler. Xi'an. Xi'an Jiaotong University Press; 2008.
[53] Zhang D, Sun G, Liu N, Yang H, Song Q, Bie R, et al. Study on the mechanism of thermal inertia action in circulating fluidized bed boiler. Appl Therm Eng 2025;267. https://doi.org/10.1016/j.applthermaleng.2025.125699.
[54] Ma Y, Li M, Wen H, Xue Y, Wang J, Lyu J. Study on dynamic evaporation rate and wall temperature of water walls in a supercritical CFB boiler during rapid hot start-up. Appl Therm Eng 2026;288:129567. https://doi.org/10.1016/j.applthermaleng.2025.129567.
[55] Zhao L, Zhou Q. The course of boiler design. Beijing: China Electric Power Press; 2013.
[56] Zima W, Nowak-Ocłoń M, Ocłoń P. Novel online simulation-ready models of conjugate heat transfer in combustion chamber waterwall tubes of supercritical power boilers. Energy 2018;148:809–23. https://doi.org/10.1016/j.energy.2018.01.178.
[57] Wang Z, Liu M, Zhao Y, Wang C, Yan J. Comparison on thermodynamic characteristics of single- and double- reheat boilers under off-design working conditions and during transient processes. Appl Therm Eng 2020;179. https://doi.org/10.1016/j.applthermaleng.2020.115620.
[58] Wang R, Tian H, Wang X, Tian R, Wu Z. Analysis of wall temperature change rate limiting supercritical CO2 power system flexibility. Energy 2025;316. https://doi.org/10.1016/j.energy.2025.134448.
[59] Trevisan S, Pathi S, Brown J, Buchbjerg B, Borrero AB, Guedez R. Thermal performance and dynamic response assessment of an industrial molten salts based power-to-heat system. Energy Convers Manag 2025;342. https://doi.org/10.1016/j.enconman.2025.120131.
[60] Shi X, Wang M, Chen C, Lu Z. Technical manual for thermal power generation equipment. Beijing: China Machine Press; 2002.